The Journal of Undergraduate Research in Physics

CONTENTS

VOLUME 1, NUMBER 1

APRIL, 1982

Published by Guilford College
for
The American Institute of Physics and The Society of Physics Students

THE JOURNAL OF UNDERGRADUATE RESEARCH IN PHYSICS

This journal is devoted to research work done by undergraduate students in physics and its related fields. It is to be a vehicle for the exchange of ideas and information by undergraduate students. Information for students wishing to submit manuscripts for possible inclusion in the Journal follows.

ELIGIBILITY

The author must have performed all work reported in the paper as an undergraduate. The subject matter of the paper is open to any area of pure or applied physics or physics related field.

SPONSORSHIP

Each paper must be sponsored by a full time faculty member of the department in which the research was done. The name, address, and phone number of the sponsoring faculty member must be included with the manuscript.

FORM

The manuscript should be typed, double spaced, on 8 1/2 x 11 inch sheets. Margins of about 1 1/2 inch should be left on the top, sides, and bottom of each page. Papers should be limited to twelve pages of text in addition to an abstract and appropriate drawings, pictures, and tables.

GENERAL STYLE

All papers must conform to the Style Manual of the American Institute of Physics. Each paper must be prefaced by an abstract that does not exceed 250 words.

ILLUSTRATIONS

Line drawings should be made with black India ink on plain white paper. If a graph is drawn on co-ordinate paper, the paper must be lined blue. Important lines should be ruled in black. Each figure or table must be on a separate sheet. Photographs must have a high gloss finish.

CAPTIONS

A brief caption should be provided for each illustration or table, but it should not be part of the figure. They should be listed together at the end of the manuscript.

EQUATIONS

Equations should appear on separate lines and may be written in black India ink.

FOOTNOTES

Footnotes should be typed double spaced and grouped together in sequence at the end of the manuscript.

SUBMISSION

Two copies of the manuscript should be sent to:

Dr. Rexford E. Adelberger, Editor
THE JOURNAL OF UNDERGRADUATE RESEARCH IN PHYSICS
Physics Department
Guilford College
Greensboro, NC 27410

SUBSCRIPTION INFORMATION

The Journal will be published biannually with issues appearing in April and October of each year. There will be two issues per volume.

TYPE OF SUBSCRIBER	PRICE PER VOLUME
SPS member	$ 3.00
Individual	$ 5.00
Institution	$10.00

Overseas subscribers add $2.00 for postage

To receive a subscription, send your name, address, and check made out to The Journal of Undergraduate Research in Physics to:

Journal of Undergraduate Research in Physics
Physics Department
Guilford College
Greensboro, NC 27410

ISSN # 0731 - 3764

The Journal of Undergraduate Research in Physics is published by Guilford College for the American Institute of Physics and the Society of Physics Students.

VOLUME 1 1982

The Journal of Undergraduate Research in Physics

Published by Guilford College
for
The American Institute of Physics and The Society of Physics Students

ISSN # 0731 - 3764

A JOURNAL FOR UNDERGRADUATE STUDENTS

For many years, undergraduate students have been frustrated while trying to get research work that they have done published in the established physics journals. These journals were designed as a place where research facutly can communciate with each other. The work of the usual undergraduate does not fit in this mission. It appeared that there was no available means for undergraduate students to communicate their research to other undergraduates.

After many years of discussion by faculty members at undergraduate institutons and by the Council of the Society of Physics Students, the Society decided to establish their own journal. The Council founded the Journal of Undergraduate Research in Physics to provide a place for undergraduate students to publish their work. An editor was appointed in 1981. A modest budget was established out of the Sigma Pi Sigma trust fund earnings, and a call for papers went out. At first the response was slow, but as the old year passed and 1982 began, this first issue began to take shape. Since that time, interest in terms of manuscripts submitted and requests for subscriptions has been increasing. It appears that this Journal is indeed an idea whose time has come.

This first issue is being mailed to each Physics Department and Library as well as SPS chapter, to announce the arrival of a new Journal. If the Journal is to survive, we will need enough subscriptions to off-set the cost of publication. We hope that each Physics Department agrees with the SPS Council and the American Institute of Physics and supports the Journal with a subscripton and encouragement to undergraduate students to publish their research work in this Journal.

As mentioned earlier, the aim of the Society of Physics Students was to produce a Journal that would be read by undergraduate students. Research done by students comes in as wide a variety as the students themselves. We intend to consider all papers. The primary refereeing is done by the sponsor of the paper. Each paper will be read by the Editor and by a panel of undergraduates. To be published, the manuscript must meet with the approval of all three. In this manner we feel that the work published will be of high quality, yet understandable by undergraduate students.

We hope to begin a department with ideas for research topics that are possible to do at small as well as large institutions. For this department to become a reality, we will need suggestions from faculty members and students from all over the country. If you have suggestions, please send them to the Journal office at Guilford College. Each suggestion will be credited to the author.

We look forward to receiving subscription requests and manuscripts from many of you in the next few months. We are currently working on the second issue of Volume 1. The deadline for submitting papers to this issue will be September 1, 1982.

Rexford E. Adelberger, Editor
Greensboro, NC

PHOTOMETRIC DISCOVERY OF VARIABILITY OF Ap STAR HD 171247

Susan King *
King College, Bristol, TN 37620

ABSTRACT

A UBV (Ultra-violet,Blue,Visible) photometric study of the peculiar type A star HD 171247 at Lowell Observatory and Kitt Peak National Observatory in June, 1981 reveals that the star varies in all three colors. We determined a probable period of 0.7928 days. However, we were not able to rule out possible periods of 1.350 days or 3.839 days.

INTRODUCTION

Our sun is a type G star which has a temperature of about 5 to 6 thousand degrees Kelvin. The type A star has a temperature of about 8 to 15 thousand degrees Kelvin, about twice that of our sun. The high temperature of the A star is responsible for its blue color. Normal A stars are not variable, that is, they do not vary in brightness. However, most peculiar A stars (Ap stars) do vary periodically in brightness, usually with a period on the order of one day, but periods shorter and longer have been observed.

Ap stars generally have intense variable magnetic fields associated with them and thus are often called magnetic stars. In addition to the peculiarities of varying brightness and an intense magnetic field, the Ap star's atmosphere apparently differs also in its chemical composition. The line spectrum of the star shows the presence of abnormal abundances of silicon, iron, mercury, chromium, europium or combinations of these elements.

The most reasonable way of explaining variations in brightness, spectral lines, and the magnetic field, is the oblique rotator model. In this theory, the star rotates about an axis which is inclined at an angle to the line of sight. The magnetic axis is assumed to be inclined to the axis of rotation. (See Figure 1) The abnormal elements are captured by the magnetic field and are located at one of the magnetic poles. Thus when the star rotates, the line spectrum will vary periodically. One conjecture is that the anomalous elements concentrate in the form of gaseous clouds above one of the poles and have a blanket effect on the star's surface. As light passes through these clouds, some of it is absorbed and re-emitted back to the star's surface. This backwarming effect produces a very hot and therefore very bright spot at the poles. This would cause the star to vary in brightness as it rotates.

OBSERVATIONS

Photometric study involves only the brightness variation of the star. The stars to be studied are chosed from a catalog of variable stars or from spectral studies which indicate that the stars are peculiar. After a star is picked, two or three comparison stars are chosen. Each comparison star is of approximately the same brightness as the variable star, of similar spectral type and is located near the variable star's position in the sky.

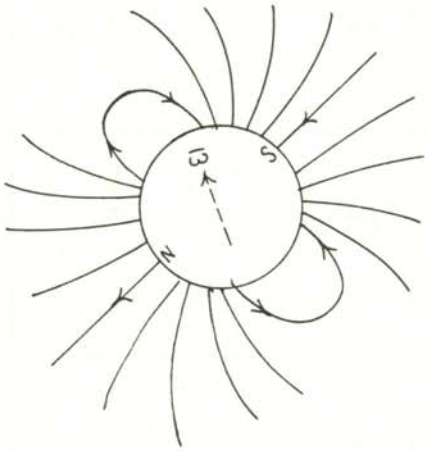

FIGURE 1
The oblique rotator model - the star rotates about an axis which is inclined to to the line of sight. The magnetic axis is inclined to the axis of rotation.

The observations reported in this paper were made during a 14 night run at Lowell Observatory using the 24 inch Morgan telescope and a 16 night run at Kitt Peak National Observatory using the #4-16 inch telescope during June of 1981. Differential photometry techniques were used. The differences were extinction corrected and transformed to the UBV (Ultra-violet,Blue,Visible) system. While obtaining data, the telescope was centered on a star and a fine adjustment made to

center the star on a small aperture so that only the light from the star could pass to the light sensitive detector (photometer). The photometer converted the photons hitting it to small electric pulses. The pulses, or photon counts, were obtained for 10 second intervals using three filters: visual, blue and ultra-violet. The output consisted of photon counts and time, recorded on paper and/or magnetic tape.

DATA REDUCTION

The magnitude of a star is a logarithmetic measure of its brightness. A derease of 1 in the magnitude means a brightness increase of approximately 2.5. The photon counts were converted to magnitudes and the difference in the

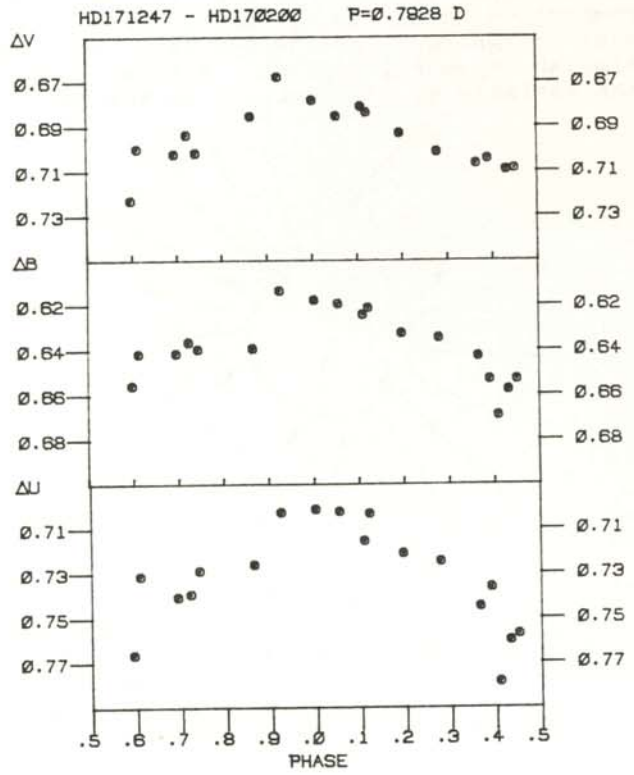

FIGURE 2
Photometric observations of Ap Star HD 171247 plotted with a period of 0.7928 days.

magnitude of the variable star and the comparison star was found. These magnitude differences for each color were then plotted against time in days. If the star had a long period of brightness variation, it might be possible to predict its period from this plot. If not, a computer program must be used to search for the period. After the period was determined, a light curve was made for each color. A light curve plots the magnitude difference versus the phase of the oscillation.

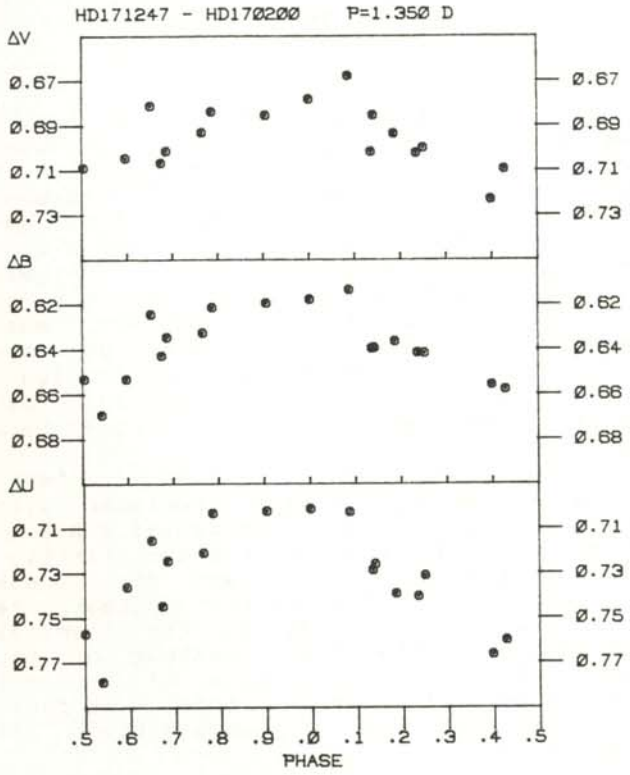

FIGURE 3
Photometric observations of Ap Star HD 171247 plotted with a period of 1.350 days.

If observations on the star were taken only once a night, several periods may appear to fit the data. To resolve which period is correct, observations must be made more than once a night.

RESULTS

Ap star HD171247 was suggested by Dr. John E. Winzer in his doctoral thesis to be a good candidate for a variable star. The star had not previously been observed photometrically. From the observations made during the summer of 1981, we found the star to be variable in all three colors with a V magnitude variation of

approximately m0.04. Since observations were made only once a night on this star, three periods appear to fit the data. We have determined a probable period of 0.7928 days (See Figure 2) but are not able to rule out periods of 1.350 days (See Figure 3) and 3.839 days (See Figure 4). The data is listed in Tables 1,2 and 3. Extensive observations of this star, taken several times a night, will be necessary to reveal which of these periods is correct.

REFERENCES Allen, Lawrence High, editor, Stellar Structure, (University of Chicago Press, Chicago), 1965

Preston, George W., "Surface Characteristics of the Magnetic Stars", Astronomical Society of the Pacific, 83, 1971

Winzer, J.E., Ph.D. Thesis, University of Toronto, 1974

*Guest Investigator, Kitt Peak National Observatory. KPNO is operated by the Association of Universities for Research in Astronomy, Inc., under contract with the National Science Foundation.

FACULTY SPONSOR OF THIS PAPER E. W. Burke, Jr. King College, Bristol, TN. 37620

ACKNOWLEDGEMENTS

Appreciation is expressed to Dr. A. A. Hoag, Director, Lowell Observatory, for providing observing time on the Morgan telescope. We are indebted to the Research Corporation for the grant which made this research possible.

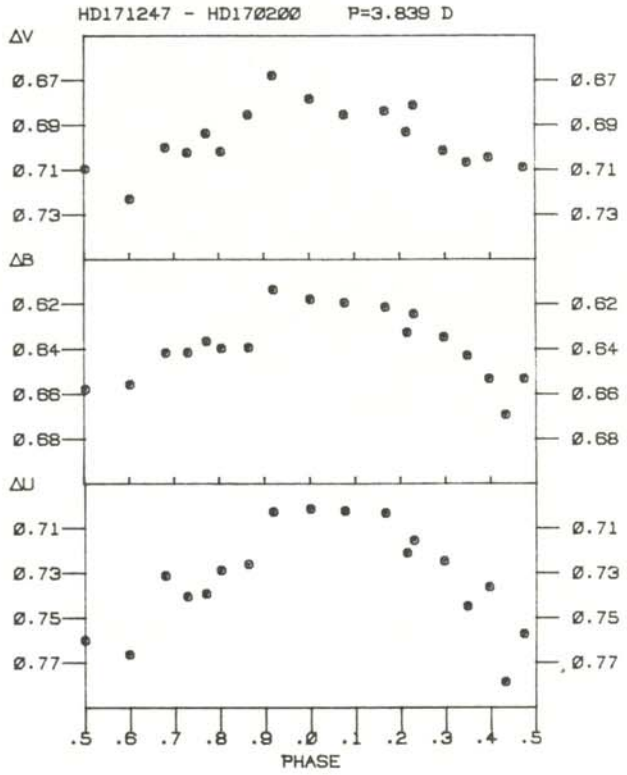

FIGURE 4
Photometric observations of Ap Star HD 171247 plotted with a period of 3.839 days.

HD171247 - HD170200 P=0.7928 D

HJD 2444000+	PHASE	VISUAL	BLUE	UV
757.9533	0.390	0.704	0.653	0.736
759.9636	0.926	0.667	0.613	0.702
760.9108	0.120	0.683	0.621	0.703
761.9309	0.407	0.000	0.669	0.778
762.8857	0.611	0.700	0.641	0.731
764.9329	0.194	0.693	0.632	0.721
765.9287	0.450	0.708	0.653	0.757
766.9155	0.694	0.702	0.641	0.740
767.9502	0.000	0.678	0.617	0.701
768.8286	0.107	0.681	0.624	0.715
769.8772	0.430	0.709	0.657	0.760
770.9015	0.722	0.693	0.636	0.739
772.9264	0.276	0.701	0.634	0.724
774.8813	0.742	0.701	0.639	0.728
775.9201	0.052	0.685	0.619	0.702
776.9597	0.364	0.706	0.642	0.744
777.9368	0.596	0.723	0.655	0.766
778.9409	0.863	0.685	0.639	0.726

TABLE 1
UBV differences for HD 171247 - HD 170200 with period 0.7928 days.

HD171247 - HD170200 P=1.350 D

HJD 2444000+	PHASE	VISUAL	BLUE	UV
757.9533	0.594	0.704	0.653	0.736
759.9636	0.084	0.667	0.613	0.702
760.9108	0.785	0.683	0.621	0.703
761.9309	0.541	0.000	0.669	0.778
762.8857	0.248	0.700	0.641	0.731
764.9329	0.764	0.693	0.632	0.721
765.9287	0.502	0.708	0.653	0.757
766.9155	0.233	0.702	0.641	0.740
767.9502	0.000	0.678	0.617	0.701
768.8286	0.650	0.681	0.624	0.715
769.8772	0.427	0.709	0.657	0.760
770.9015	0.186	0.693	0.636	0.739
772.9264	0.686	0.701	0.634	0.724
774.8813	0.134	0.701	0.639	0.728
775.9201	0.903	0.685	0.619	0.702
776.9597	0.673	0.706	0.642	0.744
777.9368	0.397	0.723	0.655	0.766
778.9409	0.141	0.685	0.639	0.726

TABLE 2
UBV differences for HD 171247 - HD 170200 with period of 1.350 days.

HD171247 - HD170200 P=3.839 D

HJD 2444000+	PHASE	VISUAL	BLUE	UV
757.9533	0.395	0.704	0.653	0.736
759.9636	0.919	0.667	0.613	0.702
760.9108	0.166	0.683	0.621	0.703
761.9309	0.432	0.000	0.669	0.778
762.8857	0.680	0.700	0.641	0.731
764.9329	0.214	0.693	0.632	0.721
765.9287	0.473	0.708	0.653	0.757
766.9155	0.730	0.702	0.641	0.740
767.9502	0.000	0.678	0.617	0.701
768.8286	0.228	0.681	0.624	0.715
769.8772	0.501	0.709	0.657	0.760
770.9015	0.768	0.693	0.636	0.739
772.9264	0.296	0.701	0.634	0.724
774.8813	0.805	0.701	0.639	0.728
775.9201	0.076	0.685	0.619	0.702
776.9597	0.346	0.706	0.642	0.744
777.9368	0.601	0.723	0.655	0.766
778.9409	0.862	0.685	0.639	0.726

TABLE 3
UBV differences for HD 171247 - HD 170200 with period of 3.839 days.

A METHOD FOR THE DIRECT MEASUREMENT OF THE STOPPING POTENTIAL IN THE PHOTOELECTRIC EFFECT

Robert W. Mielke
Sam Houston State University, Huntsville, TX 77341

ABSTRACT

A novel method is presented for the measurement of stopping potential in a photoelectric effect laboratory exercise. A very low current solid state electrometer device is used to measure the inter-electrode potential which is developed when the photocathode is exposed to monochromatic light. A stopping potential vs frequency plot yields a straight line with a slope within 1% of the accepted value of h/e.

INTRODUCTION

The photoelectric effect is a quantum effect that can be seen in experiments that an undergraduate student can perform as part of a laboratory exercise. The usual experimental method requires the use of the emitter and collector surfaces of a photodiode tube, a sensitive galvanometer, a variable DC power supply (to reverse bias the phototube), and a voltmeter to determine the voltage that is applied to the anode of the tube. A schematic of this method can be seen in Figure 1a. It should be remembered that the work function determined is that of the collector, not the emitter. (1) A major problem with the experiment is that the commercially available equipment designed for this experiment is marginal. The vacuum photodiode tube commonly used does not generate much in the way of photocurrent, usually no more than four microamperes. This is a maximum value and unless a very strong light source is used, the current produced by the tube is usually much less (10 picoamps).

To measure this small current, a delicate galvanometer, (one commercial supplier recommends the use of a galvanometrer with a sensitivity of .06 microamperes per scale division) or an electrometer is required. Both of these devices have their share of problems. It must be remembered, however, that the devices used in the old method measure the current developed by the Phototube. From this, the stopping potential of the tube must be determined by the rather complicated procedure of adjusting the current in the tube to zero or some constant value. The problem with this is that the current being measured is already quite small and hard to read with the usual equipment. The reverse current produced by the photo-emission from the collector has to be taken into account, since the collector surface is not shielded. The reverse current is determined by plotting the current produced by the tube versus the reverse voltage applied to the tube. When the bias voltage is increased, the current decreases to zero and then goes negative. As the bias voltage is increased even further, the current enters a linear region. This linear region is solely due to the reverse current for the tube.

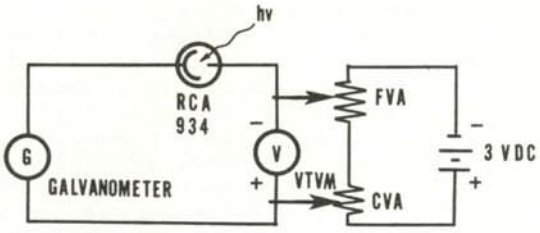

fig. 1a.

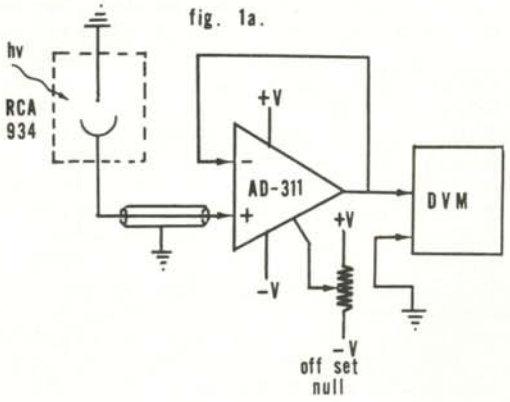

fig. 1b.

Schematics for photoelectric laboratory experiments. (a) the usual experimental arrangement using a sensitive galvanometer to measure the photocurrent. (b) the new method using the very low current AD-311 device to measure the stopping potential directly.

It can be extrapolated (linearly) back to lower bias voltages. The extrapolated curve is then subtracted, point by point, from the total current curve. The bias voltage at which the difference between the two current curves is zero is the stopping potential for the frequency of light entering the tube. This process must be performed for each frequency of light used in the experiment! The last step in the experiment requires a large amount of judgment on the part of the student, and the stopping voltage could be shifted by as much as .5 volts either way. Rather than determining either the work function of the collector or h/e, the student usually gets a lesson on how to edit and select data.

Several years ago, in a conversation between C. K. Manka and R. Biser (2), it was suggested that the stopping potential of the photodiode tube could be measured directly using an electrometer. Electrometers are rather expensive, but recent advances in electronics have led to the development of an electrometer that is stable, reliable and cheap. This device either eliminates or significantly reduces many of the problems normally associated with an electrometer. The AD-311j (a solid state ultra-low bias current varactor bridge operational amplifier) was selected for the work described here. This operational amplifier is available at modest cost from Analog Devices and has parameters which compare quite favorably with the older types of electrometers.

EXPERIMENTAL METHOD

This new method makes use of the phototube's inter-electrode capacitance. When light falls on the emitter, the photocurrent (emitter to collector) charges the collector up to some stopping potential. For this experiment, the capacitance of the tube was 1.5 picofarads. The input impedance of the electrometer is large enough (200 Terraohms) so as not to draw a significant current (.01 picoamps). As can be seen from the circuit diagram (Fig 1b), the operational amplifier is connected in parallel with the phototube, and referenced to virtual ground. The circuit is configured as a voltage follower with a gain of close to one. The equation for the voltages in this circuit is:

$$E(out) = E(in) + I(b)R(s) + E(os)$$

where I(b) is the input bias current (.01 picoamps), R(s) is the source resistance (10 gigaohms), and E(os) is the voltage drift of the amplifier as a function of temperature (30 microvolts/degree C). The contribution of these last two components are negligible since their value is below the sensitivity of the digital voltmeter that is used to measure the output voltage. The above equation becomes:

$$E(out) = E(in)$$

To calibrate the electrometer, the input is grounded and the offset null potentiometer is adjusted for an output reading of 0.000 volts DC. A standard cell is then connected to the input and E(out) is checked. If E(out) does not read the same as the known input, the null procedure is repeated again. The circuit can require as much as fifteen minutes to become stabilized, but usually is steady within 2 to 3 minutes.

EQUIPMENT

The equipment used in this experiment included several light sources , a Foci-Flex monochrometer with a 20 Angstrom resolution, several light filters (Corning glass and sharp cut-off filters), a Fluke digital voltmeter and an RCA 934 photodiode tube. The photodiode tube and sharp cut-off filters were taken from the Sargent-Welch Planck's Constant Apparatus (#2120). According to the RCA tube specification sheet (4), the photodiode tube emitter and collector are coated with a cesium-antimony compound. It was noticed early in the experiment that the box in which the tube was mounted did not offer any shielding from outside electrical interference, since it was made of wood. The tube was remounted in an all metal box and grounded.

The tube was masked with a 2 mm. slit in order to insure that the anode did not receive light directly from the source. In all probability, the anode does receive some scattered light from the source, and the reverse current will vary as the intensity squared. If this reverse current is quite large, the tube will be charged to some potential that is different from the stopping potential. The lime-glass envelope that surrounds the RCA 934 tube absorbs light at a frequency of 950 gigahertz or higher, but has a 90% transmission all through the near ultraviolet and visible frequencies.

Light sources of moderate intensity were used in an attempt to reduce the

problem of scattered light. A mercury-cadmium vapor and a mercury vapor source were used with the monochrometer and filters.

RESULTS

The data using the mercury-cadmium source and the monochrometer are shown in graph 1. The five major emission lines of the Hg-Cd source were used in the experiment. The plot appears linear in the region between 850 and 700 gigahertz, but becomes non-linear below 600 gigahertz. The slope of the linear region is within 1% of the accepted value of h/e. The non-linearity of the data at lower frequencies is a result of using a mirror

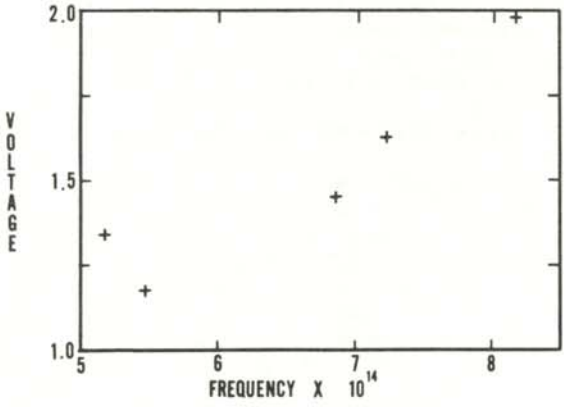

GRAPH 1.

A plot of data taken with the Hg-Cd light source and monochrometer, but no filters.

grating monochrometer to select the desired frequency of light admitted into the tube. The second order ultraviolet contributions produce non-linear data points.

Graph 2 is a plot of data using the sharp cut-off filters provided with the Sargent-Welch apparatus and a less intense Hg vapor source. With the three filters (and the fact that the tube only will react to the highest energy photons entering the tube), it is possible to obtain four reasonably spaced data points. The slope of the line obtained from this data is within 1% of the theoretical value and the intercept is an acceptable value. The work function of the tube is a bit low when compared to the value calculated from the cut-off frequency or the value listed for cesium in the CRC Handbook (5). The work function for this tube was determined to be -1.7 volts by another investigator (6) using the old method.

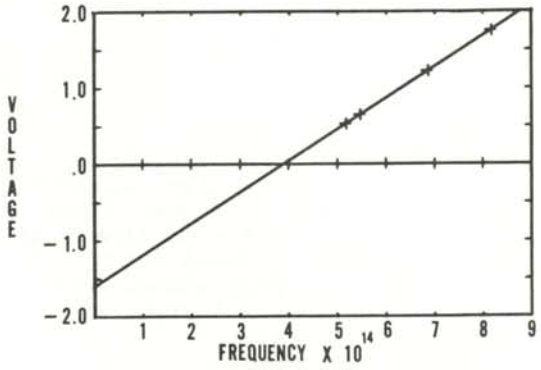

GRAPH 2.

A plot of data taken with a Hg light source, monochrometer, and "Welch" filters.

Graph 3 shows the data taken when the monochrometer and the sharp cut-off filters were used with the Hg-Cd source. In this experimental arrangement, the two highest frequency data points were taken with no filter between the light source and the monochrometer. The next data point was taken with the filter for the 4360 Angstrom line of Hg. The filter for the 5700 Angstrom line of Hg was used for the two lowest frequency data points. The cut-off filters were inserted between the light source and the monochrometer. The slope of this line is within 3.5% of the accepted value and the intercept is within .5% of the intercept determined in graph 3.

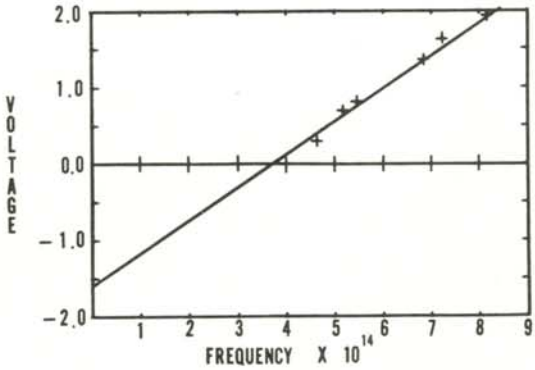

GRAPH 3.

A plot of data taken with the Hg-Cd light source, monochrometer and "Welch" filters.

CONCLUSION

The results show that this method is

a considerable improvement over the usual method of determining h/e and work function from the photoelectric effect. The circuit employed is simple, easy to calibrate, and is very stable over long periods of time. The cost of the device is within the budget of most Physics Departments.

ACKNOWLEDGEMENTS

The author would like to acknowledge the support, advice, and encouragement provided by Dr. Manka and to thank the Sam Houston State University Physics Department for providing equipment and the opportunity to pursue this research.

REFERENCES

(1) J. Rudnick and D. S. Tannhauser, "Concerning the Widespread Error in the Description of the Photoelectric Effect", American Journal of Physics, August, 1976, pp.796-798.

(2) C. K. Manka, Sam Houston State University, and R. Biser, Lamar State University. Private Communication, 1973.

(3) Analog Devices, Ultra Low Bias Current Varactor Bridge Operational Amplifier Models 310,311 Specifications Sheet, Norwood, MA., 1976

(4) RCA. Electron Tube Handbook HB-3, Photodiode Section, Harrison, N. J., 1961.

(5) C. Hodgmann, ed., Handbook of Chemistry and Physics, 42 ed., Chemical Rubber Company, Cleveland Ohio, 1961, p.2558.

(6) P. D. Jacovelli, University of Arkansas. Private Communication, 1977.

FACULTY SPONSOR FOR THIS PAPER

C. K. Manke
Sam Houston State University, Huntsville, TX, 77341

POSSIBLE CLIMATIC EFFECTS OF A LARGE METEORITE INCIDENT UPON THE EARTH 65 MILLION YEARS AGO

Jennifer A. Kuhn
Guilford College, Greensboro, NC 27410

ABSTRACT

Could a large meteorite incident upon the Earth 65 million years ago have evoked sufficient climatic change to cause the mass extinctions which have occured at the Cretaceous-Tertiary boundary? The following is a summary of a six-week summer project, the goal of which was to examine the preceding question. To properly analyze the effect of a meteorite on an ancient climate, both the meteorite itself and the environment into which it would have fallen must be understood. The climatic effects of a meteorite hitting the Earth today are first examined. Results suggest that neither dust nor water vapor thrown into the atmosphere would modify present climate sufficiently to explain global extinctions of multiple life forms. A detailed reconstruction is then made of late-Cretaceous boundary conditions, including land-sea distributiuon, sea surface temperature, topographic and vegetation changes. Using these boundary conditions, NASA's three dimensional general circulation model generates a warm, relatively cloudless and rainy Cretaceous climate.

INTRODUCTION

The question of extinctions is fascinating to consider, and the suggestion that mass extinctions of 65 million years ago (MYA) may have been caused by a meteorite hitting the earth stimulates even the feeblest imagination. It was recently discovered that the thick clay layer marking the Cretaceous-Tertiary boundary at several locations throughout the world is abnormally abundant in rare noble elements common to extraterrestrial bodies.

The possible "synoptic" impingement of these meteorites upon the earth and the extinction of great numbers and species of life forms on the earth appears to many researchers to be more than coincidence. Various theories are being formulated which attempt to draw cause-and-effect relationships between meteorites and extinctions, but weaknesses of these theories are many. Extra-terrestrial interference and extinctions may be deemed "coincident" only to within one hundred thousand to one million years. Many subtle, terrestrially-forced mechanisms could have acted to promote extinctions in that time period. Furthermore, abundance of noble elements in soil samples is not restricted to Cretaceous boundaries. The Pliocene-Pleistocene boundary is equally abundant in the same rare elements, and no signs of extinction or biologic disruption are evident. (1) At the Cretaceous-Tertiary boundary itself, it is possible to detect a lack of climate change in certain parts of the world. At the Rotone 1 formation in New Mexico, palms and sea floor assemblages are the same in the late-late Cretaceous and early Paleozoic. (2) Many references are available in the literature regarding possible reasons for extinction, and it is beyond the scope of this paper to evaluate many and varied theories.

What this paper shall summarize is our investigation of the possible climatic effects of a large meteorite incident upon the Earth 65 MYA. Our research addressed two lines of thought: first, we investigated the possible climatic effects of a large meteorite upon the Earth today. This included modelling the effects of large amounts of dust and water vapor thrown into the stratosphere upon impact of the meteorite with the ocean floor. Secondly, we reconstructed Cretaceous climates in an attempt to understand the environment into which the mysterious metorite may have fallen. We shall briefly summarize the first part of the research, in order that a full explanation of the climate reconstruction process may be afforded.

WHAT WOULD BE THE CLIMATIC EFFECTS IF A METEORITE HIT THE EARTH TODAY?

Physical Specifications of the Meteorite

Extensive research has been done to deduce the size and composition of the meteorite in question. Dimensions were calculated from the worldwide noble metal

abundances in the Cretaceous-Tertiary boundary layer, and a bolide of diameter (10+/-2) km and mass of approximately 1,000 Tkg was suggested. (3) Modelling of energy transfer mechanisms indicates the greatest efficiency for porous (cometary) objects, and chemical analysis indicates that globular bits high in chalcophile elements may be crystallized droplets from a comet of silicate, iron or ice. (4)

Dynamics of the Fall

Detailed numerical analysis has yielded information regarding the dynamics of meteor/atmosphere/ocean interactions. Speeds of 5-72 km/sec have been approximated. (5) Computer modelling indicates that a 10 km diameter meteorite would fall through an atmosphere of scale height 7.1 km without appreciable loss of energy to the atmosphere. Let us temporarily assume that the meteorite landed in the ocean (a reasonable assumption since the Earth's surface is 70% water). Ahrens (6) has calculated that a minimum ocean depth of 100 km would be necessary to stop the 10 km meteorite, such that an average ocean of depth 3 km would insignificantly slow the object, and contact with the ocean floor would be made. The effects of such a proposed fall would be twofold. The effects of dust thrown into the air upon impact with the ocean floor, and the effects of water vapor tossed into the atmosphere must be separately considered.

Dust Effects

Consider first the effects of dust thrown into the atmosphere. Estimates of the amount of particulate matter tossed into the air range from 60-100 times the mass of the meteorite (60-100 trillion tons). Calculations of transfer of meteorite energy to ejecta indicate that little (<10%) of the ejecta is lofted to heights exceeding 5 miles. Recalling that direct transfer of energy to the atmosphere and ocean while falling is quite small, and noting the small vertical range of ejecta, Ahrens concludes that most of the energy of the meteorite was channelled to the ejecta in the form of heat. The question is how effectively these hot, low-level ejecta could have warmed the atmosphere, perhaps sufficiently to affect plant and thus animal chains.

Various ways of modelling dust effects on climate were considered. The application of standard modelling techniques to the dust problem failed. Programs simulating the radiative-convective processes of the atmosphere generated multiple moist-convective layers which led to numeric instability in temperature. Thus dust effects were approximated using the results of James Pollack and Brian Toon who, also interested in the meteorite theory, have done extensive computer simulation of the behavior of dust in the atmosphere. They are currently completing studies with an aerosol model which considers optical properties of particles and possible chemical coagulations, and whose results include residence times and size distributions of the particles. Eventually Pollack and Toon wish to use a radiative-convective model to determine to what degree surface temperatures are perturbed by meteoric dust. Pollack and Toon's work is as yet unpublished, and the amount of information they felt confident in releasing was limited. Toon did disclose that though the immediate change in optical thickness of the atmosphere due to the dust distribution calculated by Ahrens was from 1 to 100, most of the ejecta fell through the atmosphere quickly, and that at the end of 3 months, a normal optical thickness was observed.(7)

This precludes the possibility that dust alone was responsible for global extinctions, for a few weeks is insufficient time for the dust to distribute world-wide. Global temperature changes can't arise without a sustained change in optical thickness. Dust may have contributed to local discomfort or extinctions, but even this must be qualified. It is a biological fact (8) that optimum environmental temperatures for most animals are much closer to their maximum possible survival temperatures than to their minimum possible temperatures. Yet, by comparison with volcanic effects, the expected direction of temperature change due to increased atmospheric dust particles is negative, i.e. towards cooler temperatures. Thus, it is difficult to attribute even local extinctions to dust effects. It is still possible that the major role of dust was to alert us that extraterrestrial substances impinged upon the Earth 65 MYA, and that the actual climatic effects were due to untraceably high amounts of water vapor.

Water Effects

Simulation of a localized high initial water content in the atmosphere was achieved with NASA's 3-D 9-layer

atmosphere general circulation model. (9) This model uses given boundary and initial conditions to solve 3-D synoptic equations that govern the whole of atmospheric wave activity. Because we desired initally to discuss the effects of water vapor on present climate only, present-day boundary conditions were not altered, and the sole initial condition modification was an introduction of great amounts of water vapor into the atmosphere.

The effects of the water vapor were analyzed with the help of monthly diagnostics presenting global, hemispheric and regional budgets for such quantities as albedo (reflectivity of the earth), radiation, precipitation, evaporation, snow cover, temperature gradients, etc., and a myriad of tables presenting dynamic parameters such as latent heat transports, eddies, fluxes, strength of circulation cells, etc. Interesting interplay between cloud distributions and albedo parameters was noted, as the cooling effect of the planetary albedo dominated the heating (greenhouse) effects of increased cloud coverage. Surface temperatures did not deviate by more than two standard deviaions from normal monthly averages. Thus, it became apparent that temperature changes due to increased concentrations of water vapor were not significant, and were certainly insufficient grounds for multiple global extinctons.

Dust and water effects were considered strictly with respect to today's climatic, geographical and topographical boundary conditions. It remains possible that there existed some distinguishing characteristics of the Cretaceous climates which would have significantly affected reactions to increased dust or water particles, and rendered the world of the dinosaur more vulnerable to extraterrestrial interferences than is our present-day world. Perhaps Cretaceous winds were stronger, and would have advected dust more quickly. Or perhaps the magnitude of the planetary albedo was significantly less in Cretaceous times, and its role in damping surface temperature changes was less dominant. To be more certain that neither dust nor water vapor could have affected a very different climate sufficiently to instigate extinctions, one must reconstruct fully the world 65 MYA, and then introduce masses of water vapor therein.

RECONSTRUCTION OF BOUNDARY CONDITIONS:

A Day with the Dinosaurs

Reconstruction of late-Cretaceous climate required the generation of various data sets to be used as boundary conditions for NASA's 3-D General Circulation Model (GCM). Land-sea distribution, sea surface temperatures (SST), topography and vegetation sets representative of 65 MYA were created based on plate tectonics, fossils, and isotope analysis. A discussion of the creation of each data set follows.

LAND SEA DISTRIBUTION

The land-sea distribution used in all subsequent data sets is based upon maps received from E. Barron. (10) The maps (See Figure 1) were drafted based on surveys of various plate tectonic maps, and are an improvement upon standard references because they represent an expanded data sample, show increased sea-floor control, and consider shallow seas. Shaded areas represent land, and the grids on Figure 1a demark present latitudes and longitudes. Comparison with present land-sea distributions is interesting. Note particularly the small Atlantic Ocean, the drifting (en route to Asia) India, the contiguous Australia Anarctica land unit, and the above-water Hudson Bay area.

Upon the suggestion of R. Fairbridge, the following changes were made in Barron's maps. (11) In North America, Virginia and the Carolinas were submerged. North Africa included extensive ocean regions not recognized by Barron. Though Australia had not yet undergone final rifting, there did exist crustal stretching 65 MYA, and upon the lowering of the crust, shallow water seas invaded. Extensive sponge fossils indicate the formation of relatively warm shallow seas covering a large part of Southern Australia. Kamchatka was also below sea level.

Sea Surface Temperatures

Sea surface temperature maps were compiled by combining knowledge of present-day distributions and variations with absolute Cretaceous temperatures generally recognized in texts (based on isotope temperatures for marine organisms), and repeated in maps by Fairbridge. Estimates of SST are particularly important, as the version of the GCM employed enlisted fixed SST, such that no initially poor guess could be

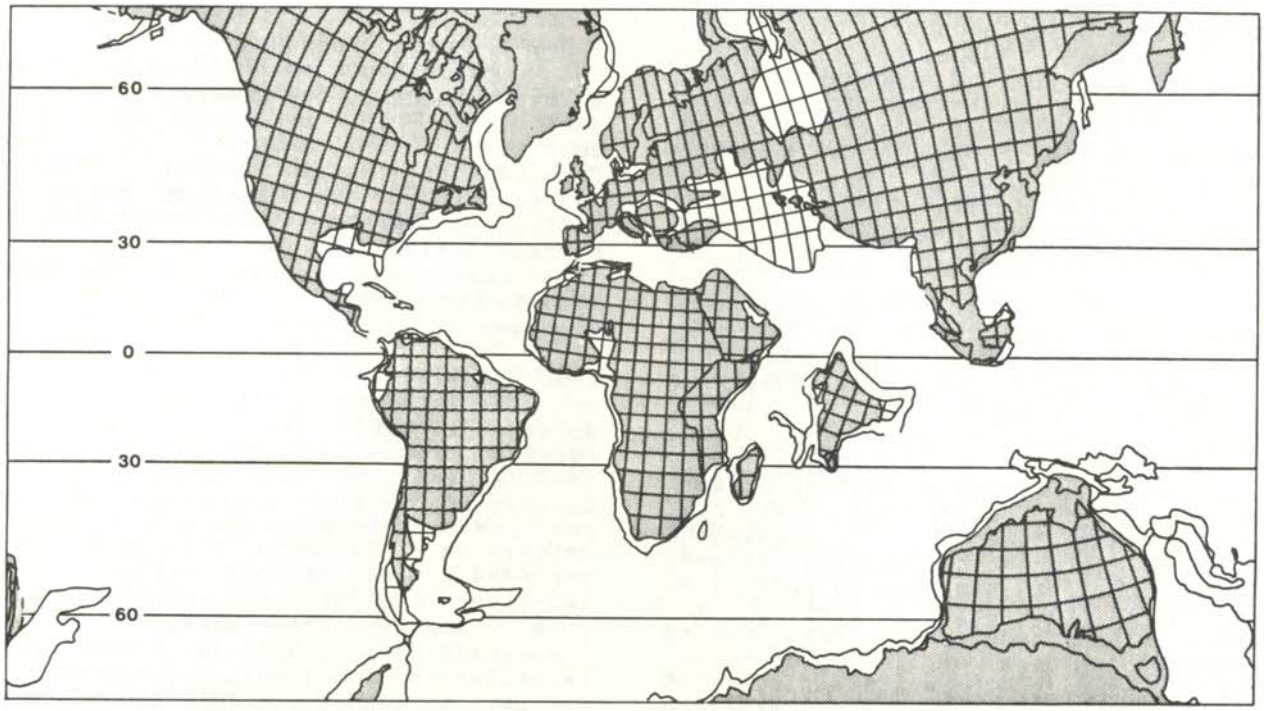

Figure 1(a)
Land-sea distributions as they were 60 MYA. The grids represent present day latitude and longitude grids.

Figure 1(b)
Processed land-sea distributions as they were seen by the computer.

TAU = 0.0 LAND COVERAGE (PERCENT) DAY 0. HOUR 0.0

		-180		-150		-120		-90		-60		-30		0		30		60		90		120		150			
LAT	J	1	2	3	4	5	6	7	8	9	10	11	12	13	14	15	16	17	18	19	20	21	22	23	24	25	26	27	28	29	30	31	32	33	34	35	36	J	MEAN
90.0	24	100	100	100	100																		100	100	100	100	100	100	100	100	100	100	100	100	100	100	100	24	100.0
82.2	23	100	100	100	100	100	70	30					10	25	25	10	10	25	25				40	50	50	70	100	100	100	100	100	100	100	100	100	100	100	100	23	69.3
74.3	22	70	100	100	100	100	100	100	100	100	100	100	100	100	100	100	100	100	85						25	100	100	100	100	100	100	100	100	100	100	75	60	60	22	92.7
66.5	21		10	15	20	15	40	100	100	100	100	100	100	100	100	100	100	100	100	60		10	50	33	15	95	100	100	100	100	100	100	95	60	20				21	72.4
58.7	20							25	100	100	100	100	100	100	95	80	100	75	50	100	100	100	40			75	100	100	100	100	100	100	50						20	87.1
50.9	19							5	100	100	100	100	100	100	50	75	40	20	80	80	100	85	80	87	77	100	100	100	100	100	100	85	30						19	80.2
43.0	18							15	100	100	100	100	100	100	70	2	16	60	60	75	80	20	13	70	100	100	100	100	100	100	40							18	71.7
35.2	17							80	100	97	88	80	25	20				60	70	80	50	25		13	50	100	95	100	100	92	20							17	67.2
27.4	16							35	100	16	25	13				4	30	15	25	40					10	15	100	100	33									16	37.4
19.6	15							5	80	50	25	13				25	95	70	30	25	4						84	66										15	44.8
11.7	14								40	20	25					80	100	100	100	100	92						60	80	25									14	69.2
3.9	13										45	50	4			85	75	75	100	100	60	70	4	5			20	95	40									13	55.2
-3.9	12										100	100	70	6	30	40	60	100	80	30			30	13				15	2									12	51.9
-11.7	11										20	100	100	100	98	15		60	100	100	40			40	87													11	75.0
-19.6	10										9	80	100	100	87			45	100	100	30			85	30													10	70.4
-27.4	9											50	100	95	45			55	100	100	30	40		30						5	15							9	55.4
-35.2	8											80	100	55				33	100	75	10	30								50	90							8	62.3
-43.0	7											80	40					12	75	12								25	80	100	100	40	4					7	51.6
-50.9	6	20										60																100	100	100	60	30	75					6	68.9
-58.7	5	40										2																75	20	5	10	25	75					5	31.5
-66.5	4									12	60						20	20	20	25	30	55	55	45	40	75	80	75	75	75	70	45	25	2				4	45.4
-74.3	3	20	25	33	40	50	50	65	70	65	95	85	15		7	50	95	100	100	100	100	100	100	100	100	100	100	100	100	100	100	100	100	90	20	10	10	3	71.3
-82.2	2	100	100	100	100	100	100	100	100	100	100	100	100	100	100	100	100	100	100	100	100	100	100	100	100	100	100	100	100	100	100	100	100	100	100	100	100	2	100.0
-90.0	1	100	100	100	100	100	100	100	100	100	100	100	100	100	100	100	100	100	100	100	100	100	100	100	100	100	100	100	100	100	100	100	100	100	100	100	100	1	100.0
LAT	J	1	2	3	4	5	6	7	8	9	10	11	12	13	14	15	16	17	18	19	20	21	22	23	24	25	26	27	28	29	30	31	32	33	34	35	36	J	65.2
		-180		-150		-120		-90		-60		-30		0		30		60		90		120		150			

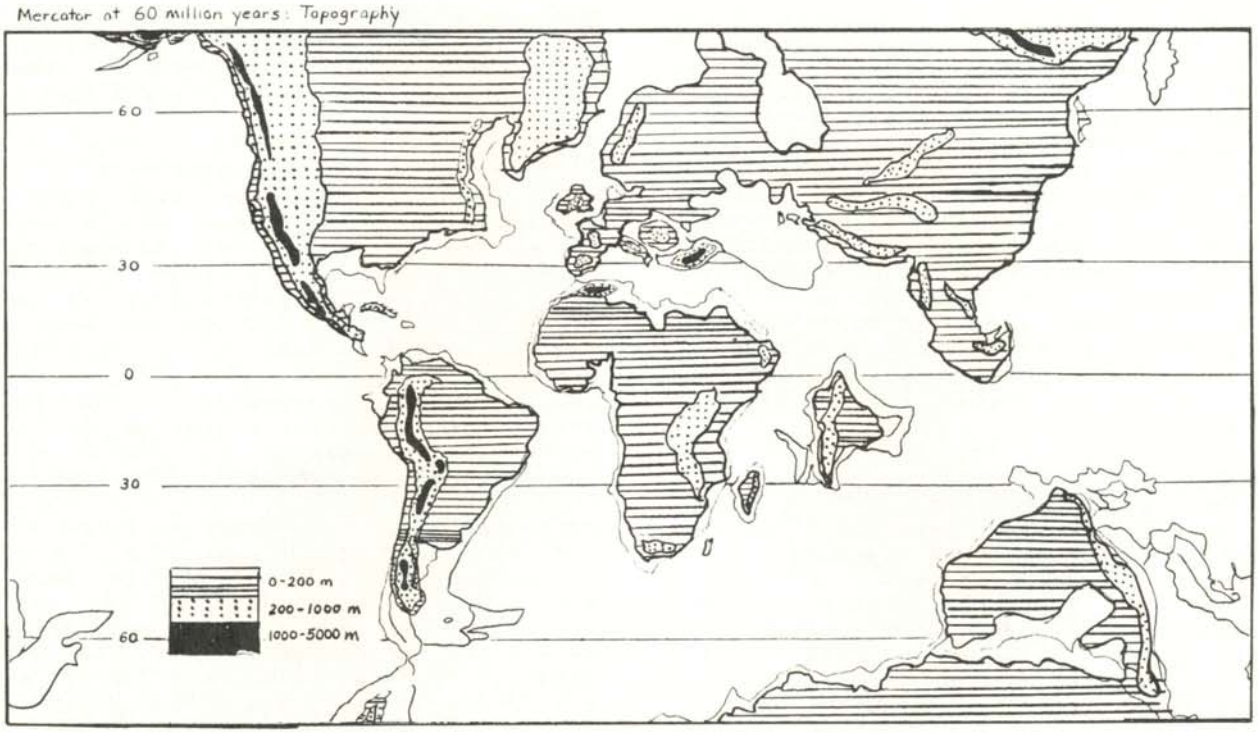

Figure 2
Topographic map of the world 65 MYA. Notice a largely smooth surface with little volcanic activity or continental mountains.

reversed or compensated for dynamically with time. Because there exists absolutely no firm evidence of glaciation during the Cretaceous, average sea-surface temperatures at the poles were set to be greater than zero. This did not preclude seasonal glaciaton, but did prohibit the growth of ice sheets thought to have been absent 65 MYA. Globally, SST averaged several degrees higher in the late Cretaceous era (12). Estimates are based on highly temperature-selective coral reefs and on vegetation patterns. Modern temperature distributions, such as maxima about the equator, were retained. Once average annual SST were obtained, monthly values were generated. Using May and November as months of zero deviation of the (latitudinal) zonal mean SST from the annual mean, and February and August as months of maximum deviations, we assigned monthly deviations from zonal mean as a function of latitude. (13) (This required fitting sine curves to functions with minima (zero's) at months 5 and 11, and maxima (latitudinally dependent) at months 2 and 8.) (14)

One may question using present day SST ranges, and even argue that increased temperatures (such as those of the Cretaceous) imply decreased mixed layer depths and thus increased SST variations with season. Because such qualitative argument is itself somewhat speculative, Occam's razor was wielded, and present-day deviations were applied.

TOPOGRAPHY

Topography and vegetation data sets were based almost exclusively on maps drafted by Rhodes Fairbridge expressly for this project. Global maps of topography and vegetation for late Cretaceous periods did not previously exist, and a piecemeal collage of assorted textbook descriptions seemed insufficient. Fairbridge's maps are consistent with textbook descriptions, yet go beyond any previously-existing collection in scope and continuity.

Topographic maps (see Figure 2) indicate a largely smooth, virgin surface. There was little volcanic activity or continential mountain building in the

world until differential mountains began to form in the Laramide orogeny at the end of the Cretaceous. Uplift that was present tended to occur in recently rifted margins. Downwarp resulting from continental spreading (recall the shallow Australian seas) was followed by local upwarp and splitting (e.g., the contemporary Red Sea region). Such uplifting did not yield sites of great elevation, though 1000+ meter regions are to be expected.

Mountain heights as indicated on the maps are based on sediments from the mountains. Lack of glaciation and glacial deposits suggest the 5000 meter limit on mountain heights.

VEGETATION

Because reflectivity varies highly with vegetation type, detailed knowledge of vegetation patterns was necessary. (15) Vegetation studies indicate widespread deciduous and evergreen forests extending to within 20 degrees of the poles. (See Figures 3 and 4). There existed no ice caps at the poles, but simply tundra. Deserts were scarce. Vegetation patterns suggest a warm, moist equable climate with sufficient precipitation to host widespread rain forests, and sufficient light to nourish evergreens at 70 degrees North.

PREPARATION OF BOUNDARY DATA SETS

Boundary condition data sets were processed and prepared for the GCM in the following fashion: a medium resolution 8 degree x 10 degree (longitude x latitude) grid was laid upon each graph, and various distributions were computed for each box. The percentage of land within each box was estimated. The SST of any box containing water was approximated. The average height of the land contained within each box was calculated by estimating the percentages of 0-200, 200-1000, and 1000-5000 meter land in each box, and weighing these percentages by factors of 100, 400 and 2000, respectively. Finally, the percentage of land within each grid box was expressed as the sum of the percentages of land of the eight different vegetation types employed in NASA's GCM: desert, tundra, grassland, grass/shrub, grass/tree, deciduous, evergreen and

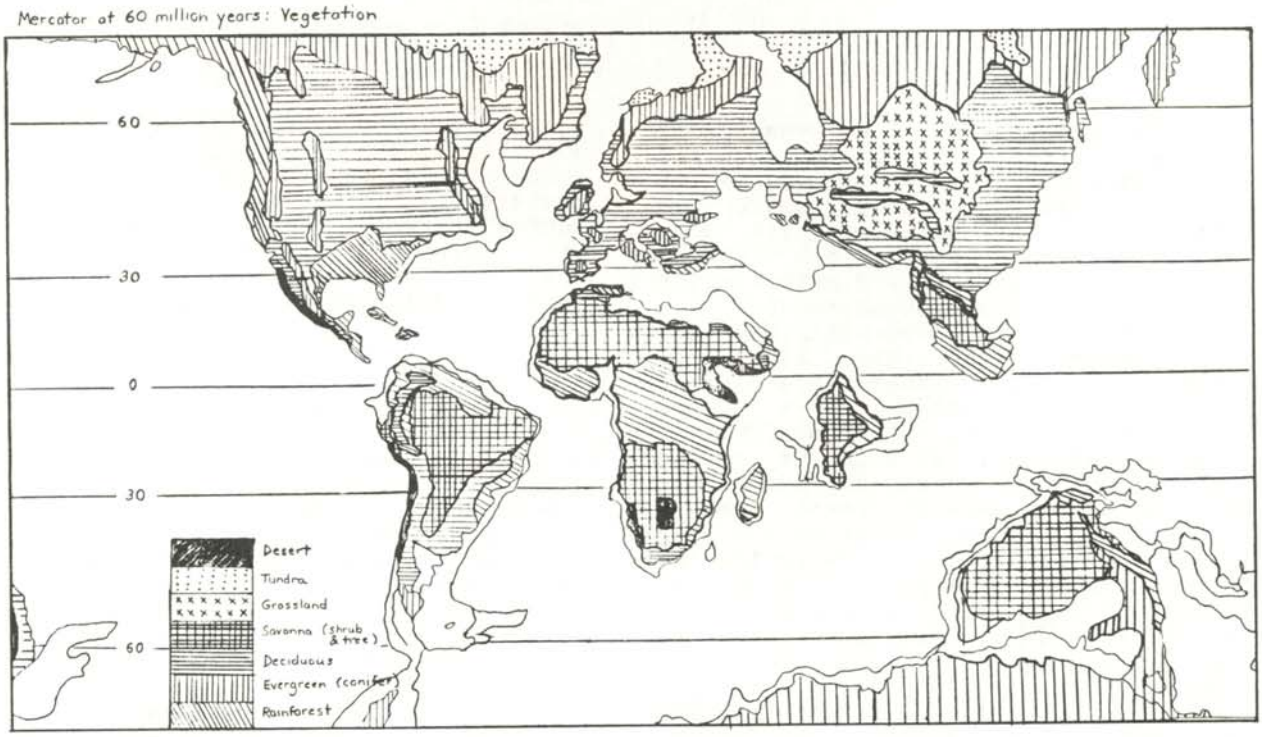

Figure 3
Vegetation map of the world 65 MYA

rainforest. The type which the maps indicate as "Savanna" is a combination of the two separate categories, grass/shrub and grass/tree.

To give the reader a feeling for the data sets resulting from the various maps, we have included Figure 1b. This is a processed data set which shows the land coverage data as the computer would recognize them - nothing more than a series of numbers and percentages of land within various regions. Comparison between Figures 1a and 1b may also give the reader a feeling for the resolution of an 8 degree x 10 degree grid.

INITIAL CONDITIONS

Upon completing the boundary condition data sets, it was necessary to formulate initial conditions for both the atmosphere and the ground. Atmospheric boundary conditions included extremely weak random winds, relative humidity of 50% everywhere, and arbitrary clouds and pressure. Ground temperatures varied gradually from 0 degrees C at the poles to 26 degrees C at the equator, as did the mean annual temperatures in Thompson and Barron's work (16). The polar limit of 0 degrees C was established to prohibit significant ice formation, as was previously mentioned with respect to SST. Isotope studies (Shackelton, 1979) deny that tropical temperatures of the Cretaceous exceeded those of present-day, such that adopting today's annual equatorial temperature was acceptable. The 0 to 26 degree C temperature gradient was initially imposed at all nine atmospheric layers. Isothermal initial conditions are not uncommon in modelling climates, and guessing a more representative distribution would have been unwarranted.

Specifiying ground conditions included prescribing snow amounts for ocean ice, earth and land ice, specifying first and second level of the ground temperatures for these three ice types, specifying ice and water contents in ground layers 1 and 2, and specifying snow ages. All parameterizations dealing with snow or ice were set to zero. Level one earth temperatures were specified as explained. Level two earth temperatures were set 10 degrees C cooler than the surface (level 1) temperatures. Amounts of water within the earth were set to 50% of the water field capacity of each grid box.

RESULTS

Upon completion of boundary and initial condition data sets, the GCM was run. Such detailed synoptic knowledge of the variables and indicators within the world climate system allowed the multiple and simultaneous solution of various dynamic energy and momentum transport equations. (17) The climate run was initiated on 1 December Cretaceous Standard Time (CST) and generated data and monthly diagnostics until surface conditions caused the program to stop in mid-August, CST. Recalling how greatly surface conditions had been altered from

Figure 4
North Pole sterographic map of the earth 65 MYA showing vegetation. Notice the lack of an ice cap.

present-day conditions (e.g., the topographic boundary conditions and the ground initial conditions), it is understandable that difficulties would arise in that particular area. Significant conclusions can be drawn through comparison of typical modern-day climate parameters to those of the first seven months of Cretaceous climates.

Table 1 compares seven major parameters for the first seven months of the year in present day (822) and Cretaceous (828) climates. All values are global averages. Over the first seven months, Cretaceous climates were an average of 7 degrees warmer than are modern-day climates. Precipitation increased significantly (over 6%), balancing increased evaporation at higher temperatures. No ocean ice or land ice was generated, and though snow cover reached 12% in the Northern Hemisphere in January, and 12% in the Southern Hemisphere in July, the snow completely melted in the summer seasons in both hemispheres, such that snow cover dropped an average of 6.7%. An ice-free Cretaceous appears possible. (18) It is also possible that two complete years of diagnostics should be generated before presuming sustained summer thawing of snow; perhaps snowing at all, with rather warm December initial conditions, is significant.

	Planetary Albedo (%)			Surface Temp (°C)			Total Cloud Cover (%)			Total Precip (mm)			Atm H_2O (mm)			Total Snow Cover (%		
	828	822	P.A.	828	822	S.T.	828	822	T.C.C.	828	822	T.P.	828	822		828	822	T.S.C.
Jan	28.8	30.9	-2.1	20.7	12.1	8.6	48.7	52.1	-3.4	3.7	3.0	0.7	47.8	23.1	24.7	5.9	14.6	-8.7
Feb	25.4	30.0	-2.8	19.8	12.3	7.5	46.4	51.3	-4.9	3.6	3.0	0.6	36.0	25.5	13.5	5.6	14.4	-8.8
Mar	25.2	29.6	-4.4	19.7	12.9	6.8	45.6	50.4	-4.8	3.6	3.0	0.6	33.3	23.7	9.6	5.1	13.2	-8.1
Apr	25.4	29.4	-4.0	20.1	13.8	6.3	45.8	49.4	-3.6	3.7	3.0	0.7	33.0	23.8	9.2	3.8	10.8	-7.0
May	25.3	30.8	-5.5	20.6	14.5	6.1	45.5	51.5	-6.0	3.9	3.2	0.7	34.5	25.1	9.4	3.3	8.9	-5.6
June	25.3	30.5	-5.2	21.1	15.0	6.1	45.3	52.1	-6.8	3.9	3.3	0.6	31.6	26.5	5.1	2.3	7.3	-5.0
July	25.0	30.0	-5.0	21.3	15.3	6.0	44.5	51.9	-7.4	3.8	3.2	0.6	35.3	26.6	8.7	2.5	6.9	-4.4

Table 1
Comparison of Cretaceous and present day parameters determined by the model. 828 are the Cretaceous data and 822 the present day (control) data.

Though there were much greater amounts of water in the atomosphere (+11%) during the Cretaceous, total cloud cover and planetary albedo dropped by greater than 5% and 4% respectively. The decrease in total cloud cover with increasing temperature is consistent with results of dynamic studies by Wetherald and Manabe (1975) and others. More generally, all of the preceding statistics are consistent with standard literature on Cretaceous climates. This is to be expected, since they were generated from boundary and initial conditons based on the literature. The wealth of new information, then, comes in examining newly-generated parameters not directly observable from isotope studies, fossils and sedimentations. An investigation of the dynamics of the Cretaceous atmosphere is in order. A thorough investigation of dynamics was not made, though a weaker jet stream and circulation cells were noted. We initially postulate that these may be due to the weaker temperature gradient. Low Aleutian pressure zones appeared, just as they do today. Detailed study of latent heat transport, radiation flux, and wind velocity diagnostics is encouraged.

Before concluding this examination of Cretaceous climate, one must consider the plausibility of one particular aspect of vegetation. Is it indeed possible for forests to extend north of 70 degrees North, even given sufficiently warm (Cretaceous) temperatures? Light as well as temperature budgets are of prime importance to plant physiology. There exists a limit called the light compensation point (lcp) below which plants cannot produce sufficient food by respiration processes, and begin to "eat themselves up", quite literally drawing upon internal resources for nourishment. Unless plants go completely dormant, they consume themselves in the absence of sufficient light. Low temperatures, not high, promote dormancy. Low temperatures were certainly not present 65 MYA, and dormancy mechanisms were not triggered. Furthermore, as temperatures increase, light compensation points and thus light (food) requirements increase, so that more light was required of trees at 70 degrees North in the warm Cretaceous period than

would currently be required by trees at the same latitude. (19)

Jack E. Wolfe has demonstrated (1980) that the current 50 degree North latitude limit of broad-leaved evergreens is indeed due to light levels and not to temperature. (20) This presents the question of how Cretaceous trees, which required more light for survival, could have lived at higher latitudes. Either plant physiology was different 65 MYA, or more light was indeed incident at high latitudes. If the former is true, then isotope dating methods are invalid, for the basic assumption of isotope dating is that the same chemical reactions have governed plants and animals throughout time. "Knowledge" gained thus far from isotope studies is a difficult thing to toss out. Perhaps, then, light budgets were different 65 MYA. We have identified a decrease in planetary albedo, such than an average of 4.1% more light was incident globally than is today. At 74 degrees North in particular, planetary albedo was 14% less 65 MYA than it is today. (The visual component of planetary albedo was 17% lower, and the near infrared component was 9% lower.) Surface albedo decreased by 19% (visual, 29%; near infrared, 3%). Short-wave (SW) atmospheric absorption increased by only 6% at 74 degrees North latitude, and 8% more light was incident at 74 degrees North in Cretaceous times than today. Whether this is a sufficiently high light increase to sponsor the various species of conifers represented by Cretaceous fossils must be left to the botanists to decide.

Light budgets could also have changed for less subtle reasons, such as the decrease in obliquity to 10 degrees. Though such a change in the earth's tilt would imply an enormous change in angular momentum, different types of evidence seem to indicate the variation of certain parameters, and obliquity in particular, over geologically long periods of time. (21) Though no theory yet satisfactorily presents a physical forcing mechanism to explain large changes in obliquity, we did not want to discard a possible explanation for varying light budgets. Thus we changed the obliquity boundary condition to 10 degrees, and simulated Cretaceous climates for most of the month of January, CST. Though snow cover decreased by 1.9%, all other parameters identified in Table 2 changed only slightly. The differences between Cretaceous and modern climates were without exception greater than those between Cretaceous with 23.5 degrees obliquity and Cretaceous with 10 degrees obliquity. It appears that subtle atmospheric changes more fully explain the existence of trees at high latitudes than do severe alterations of planetary rotation.

January	Planetary Albedo	Surface Temp	Total Cloud Cover	Total Precip	Atm H_2O	Total Snow Cover
Present Day	30.9	12.1	52.1	3.0	23.1	14.6
Cretaceous I ($23\frac{1}{2}^\circ$ obliquity)	28.8	20.7	48.7	3.7	47.8	5.9
Cretaceous II (10° obliquity)	28.7	21.7	48.3	3.6	48.6	4.0

Table 2
Comparison of Cretaceous and present day parameters with different angles of obliquity. The temperature is in C, precipitation and atmospheric water in mm and the rest are percentages.

CONCLUSION

This concludes our separate examinations of meteoric impact effects and of ancient climates. The climatic effects of a meteorite seem to be much less significant than various proponents of extinction theories expound. In addition, entirely new knowledge of dynamics of ancient climates has been generated, if not yet sufficiently analyzed. Ideally, a third facet to our research would have been combining knowledge of meteoric impact and of Cretaceous climate to speculate on the effects of the meteorite in that paleoclimate. Time did not permit the full integration of our resouces, i.e. the introduction of high initial water vapor content to the Cretaceous environment modelled by the GCM. Conclusive results await further computer runs. The information gained from work thus far is significant, however, both with respect to (negative) development of a particular extinction theory, and increased understanding of one specific palaeoclimate.

ACKNOWLEDGEMENTS

This paper resulted from a summer research project carried out by Jennifer Kuhn at the Summer Institute for Planets and Climate, sponsored by Columbia University in conjunction with NASA Goddard Institute for Space Studies. Kuhn's advisor throughout the project was Dr. David Rind.

We thank Dr. Eric Barron (NCAR) for providing us with as yet unpublished maps of the Cretaceous land-sea distribution, and Dr. Thomas Ahrens (Caltech) for his estimates of dust and water vapor distributions in the atmosphere. We owe a huge debt of gratitude to Dr. Rhodes Fairbridge (Columbia) for sketching the sea surface temperature, topography and vegetation maps, and being repeatedly available to answer the geological queries of a physics student.

We would also like to thank many people at GISS for their assistance throughout the project. Reto Ruedy, Bob Suozzo, Gary Russell and Lie-Chang Tsang were especially helpful with the creation of the data sets and the mechanics of the operations of the model. Fellow students Harold Brooks and Leonard Smith provided helpful discussions, and combined numerous technical suggestions with continual moral support. We thank you all.

REFERENCES

(1) Frank Kyte, Zhiming Zhou and John T. Wasson, Nature. 292,5822 (1981).

(2) Jack A. Wolfe, Personal Communication.

(3) John D. O'Keefe and Thomas J. Ahrens, "Impact Mechanics of the Cretaceous-Tertiary Extinction Bolide," preprint. Four independent calculations of the size of the impacting object are indicative of or consistent with a bolide of diameter (10 +/- 4) km. See Luis W. Alvarez, Walter Alvarez, Frank Asaro, Helen V. Michel, Science. 208,4448 (1980)

(4) Science News. 120,3 (1981).

(5) O'Keefe and Ahrens, "Impact Mechanics of the Cretaceous-Tertiary Extinction Bolide", preprint.

(6) Ibid.

(7) This information was disclosed by James Pollack in a personal communication between Pollack and James Hansen, director of GISS, and principal coordinator of the Summer Institute.

(8) Cesare Emiliani, EOS. 61,23 (1980).

(9) Hansen et al., "Efficient 3-D Models for Climate Studies: Models I and II", in preparation.

(10) Eric Barron, Personal Communication, maps in press.

(11) Rhodes Fairbridge, Personal Communication.

(12) L. A. Frakes, Climates Throughout Geologic Time (Elsevier, Amsterdam, 1979).

(13) Based on the Dual SST Map Set prepared by Todd Williams (GISS), April 30, 1981.

(14) Monthly SST values were generated by a program written by Harold E. Brooks, a fellow Summer Institute student.

(15) Vegetation type is also important because the water capacity, i.e., the ability of a region to retain water, varies with vegetation type.

(16) Stanley L. Thompson, Eric J. Barron, J. of Geology. 89,143 (1981).

(17) Barry Saltzman, Advances in Geophysics 20 (1978)

(18) Eric J. Barron, Stanley L. Thompson, Stephen H. Schneider, Science. 212,4494 (1981).

(19) Jack A. Wolfe, Personal Communication.

(20) Jack A. Wolfe, Palaeogeography, Paleoclimatology, and Palaeoecology, 30,313 (1980)

(21) See George Williams' Megacycles (1981), wherein a Precambrian obliquity of 60 degrees is deduced, based on geological evidence.

SPONSOR OF THIS PAPER

David Rind
Goddard Institute for Space Studies, 2880 Broadway, New York, NY 10025

MORPHOLOGY OF M8

Jonathan Marr and Douglas Rosinski
University of Rochester, Rochester, NY 14627

ABSTRACT

A morphological study of the hourglass in M8 was undertaken in the radio, infrared, and visual parts of the spectrum. We used new and originial measurements in the infrared, photographic infrared, Hα, and blue, and data taken from the literature. Models and explanations for the hourglass are investigated and the possibility of the presence of protostars within the hourglass is suggested.

INTRODUCTION

The nebula M8 (also known as NGC 6523 and the Lagoon Nebula) is a very complex area of gas and dust of great interest to astronomers as a region of recent and perhaps current star formation. We have undertaken a study of the central part of the nebula through a collection and interpretation of data in the radio, infrared and visual parts of the spectrum. Our data consist of findings discussed in the literature as well as originial observations in the visual and infrared. We discuss here our results and give an overview of the region studied. We also propose ideas for future work.

M8, along with M16, M17 and M20, make up a group of nebulous regions in the Sagittarius arm of our galaxy approximately two kiloparsecs away, between us and the galactic center. It is characterized by three distinguishable regions: a cluster of Type O stars (young, very hot stars) in the East known as NGC 6530; a dense band of dust running north-south dividing M8 into halves; and in the west, a large molecular cloud of dust and gas with an unusually small intense cloud of ionized hydrogen that is emitting radiation (known to astronomers as HII emission) in the shape of an hourglass. The exceptionally large number of Type O stars in the eastern portion (NGC 6530) indicate that much star formation must have occurred there relatively recently. But there is also a low dust density there, so there is not enough material remaining for new stars still to be forming. The extra dust and gas were probably blown off by the new hot stars. In the West, however, we find the presence of few Type O stars, but a high dust density. Thus, as has been postulated by Thackeray and others, it appears that star formation has migrated from HGC 6530 in the East westward to the hourglass region, where star formation probably is still in progress.

The hourglass and the surrounding area are the objects of our investigation. The hourglass is a small optical region of ionized hydrogen (HII region) running north-south. To cause the hydrogen to be ionized, a high energy source (such as an Type O star) is needed. Just to the West and in line with the waist of the hour glass is a very young Type O star known as Herschel 36. A little to the north-east are two other Type O stars, Cordoba 12403 and Sagittarius 9, an SAO star (see Fig 1). Usually a HII region surrounds a Type O star spherically, but here we find the H II region next to the Type O stars, not surrounding them. This is one thing that we have attempted to explain in our investigation.

OBSERVATIONS

Due to inconsistencies in the literature, we first had to determine the positions of the stars Herschel 36 and Cordoba 12403. Using a photograph of the area, a measuring machine (Mann machine), and the known positions of the SAO stars within the photograph, we used a least squares method of triangulation and found the positions to be:

Her 36 18h 00m (36.12+/-.05)s
-24degrees 22' (52.46+/-.05)"

Cor 12403 18h 00m 42.04s
-24degrees 21' 59.59"

Image tube plates taken at Kitt Peak (13) by Sharpless (4) at Hα (6563 Angstroms), blue (4500 Angstroms), and Photographic infrared (7800 Angstroms); infrared emission data at 2.2 microns, 3.28 microns, and 3.5 microns obtained by Pipher and Willner (1); and data taken from the literature constitute the

observations used in our studies. (2)

At Kitt Peak, each of the plates taken by Sharpless was scanned by a scanning microphotometer. Each 40 micron x 40 micron pixel of the plate was converted into a digitized value for the relative intensity, and stored on magnetic tape. At the University of Rochester, the data on the tape were converted into relative intensity levels. In this manner, isophotal contours (lines of constant intensity) were drawn for each plate. In Figure 2 we present the contour map of Hα. The maps were then transferred

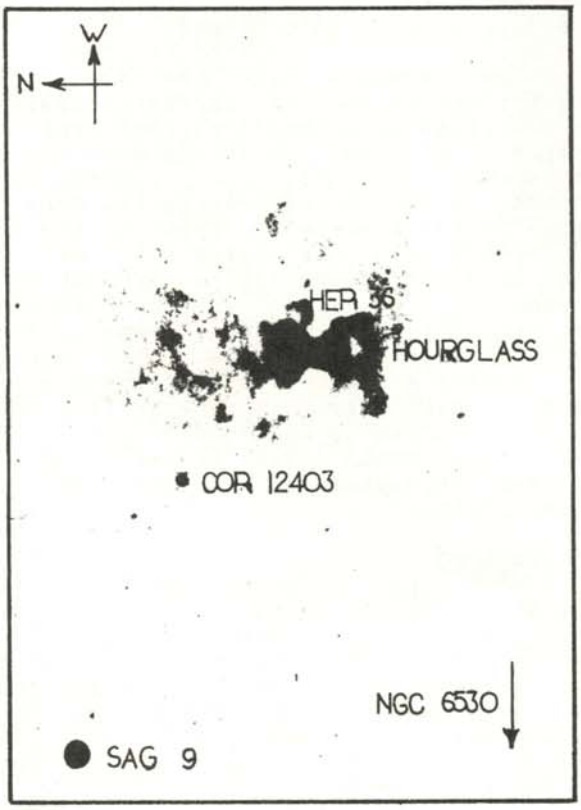

Figure 1
Photograph of the hourglass region of M8 showing the location of nearby Type O stars. The plate was taken at Kitt Peak at Hα with an exposure of 10 seconds using a Carnegie Image Tube.

to acetate transparencies so that comparisons of emission contours could be made by simply overlaying the maps at the wavelengths of interest. The emission data in the infrared taken by Pipher and Willner and data taken from the literature were converted to the same scale and drawn on transparencies.

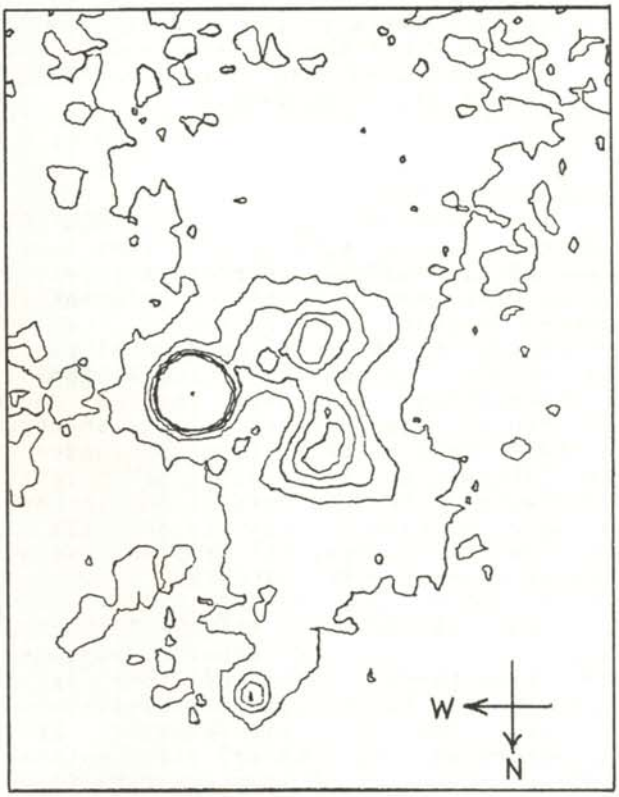

Figure 2
Contour map of the hourglass region in M8 in the Hα spectral region. The lines are isophotal contours of a plate taken by S. Sharpless at Kitt Peak

The infrared observations of Pipher and Willner were used to calculate the color temperatures of the dust associated with the hourglass. We then had a color temperature map (Fig 3) to compare with the previously mentioned maps.

RESULTS

Emission Peaks

Thackeray (3), in his investigation of ionization fronts in HII regions, studied the hourglass in detail and found

each of the lobes to have three main condensations with stellar characteristics of roughly the same size. The northern lobe, however, has one large condensation. Zeilik found emission peaks at 2 microns and 24.1 GHz in the northern lobe only. Dyck also found peaks in the northern lobe at 11 microns, and Turner et. al. at 2695 MHz. Thus, at the longer wavelengths, emission peaks have been found in the northern lobe, but no corresponding peaks in the south. (2) Our observations in the visual, however, showed equal intensities in the two lobes (Figure 2). In the visible wavelengths, the hourglass appears symmetrical, while at longer wavelengths, a higher intensity in the northern lobe is observed. Could this be an indication of condensation such as a protostar in the northern lobe? If so, we should see a "hotspot" in the position of the protostar in the near infrared wavelengths over the background temperatures caused by Her 36. In Appendices I and II are the results of our calculation of the color temperatures of the dust in the hourglass derived from the infrared emission data at 2.2 microns and 3.5 microns taken by Pipher and Willner. Unfortunately the results show no such "hotspot". Instead we only found a higher than expected dust temperature to the east of Her 36.

Relation of the Hourglass to Her 36 and Cor 12403

Thackeray (2) discussed an apparent physical connecting bridge between Her 36 and the northern lobe seen on a 5 minute red exposure, and a winding extension of the southern lobe apparently connected with Cor 12403. The connections gave the appearance that Her 36 and Cor 12403 are located within the nebula, rather than in the background as previously believed. In our visual observations, we found a line of high intensity connecting Her 36 and the northern lobe (Figure 2), though we did not find any connection between Cor 12403 and the hourglass.

Expansion Rates

Smith and Weedman (4) determined the expansion rates of the lobes through investigations into the twice-ionized oxygen (OIII) line splitting. OIII emission is found in the outer edges of HII emission regions, the boundary between ionized and non-ionized hydrogen. Their results showed expansion rates of 20 km/sec and 13 km/sec for the northern and southern lobes respectively. The different expansion rates are another point that must be considered in an explanation of the hourglass.

DISCUSSION

It had been hypothesized that the hourglass could be a bipolar reflection nebula. But since we find emission peaks in the infrared and radio just in the northern lobe, and through polarization measurements, we find the peaks clearly to be caused by emission and not reflection of radiation, we must rule this possibility out. If it were bipolar, the lobes should be symetrical at all wavelengths.

Pottasch (5) discussed the idea that Sagittarius 9 could be the primary source for the ionization in the Hourglass. Sag 9 is the brightest star in the area and certainly can supply enough energy. But, along with many others (6), we find this unlikely. Sag 9 is not located near the center of density. It possesses a radial velocity of +9 km/sec compared with an average of -6 km/sec for the other stars associated with the nebula. (5) Finally, there is no supporting observation such as the apparent connections between Her 36 and Cor 12403 and the lobes of the hourglass.

Her 36 and Cor 12403 appear to be the most likely energy sources. But one must explain the asymmetrical placement of the HII region to the East of Her 36. Any correlation of Her 36 or Cor 12403 to the excitation of the hydrogen in the hourglass must account for the fact that the HII region is next to Her 36 and further from Cor 12403, not symetrically located around one or both of them. This could be due to foreground dust obscuration (7). The hourglass could be a hole in a dense cloud of dust obscuring the rest of a spherical HII region. To check this, we determined the extinction coefficient for the dust. The extinction coefficient, defined by the equation

$$\text{Flux observed} = \text{Flux of source} \times \exp(-\tau)$$

is a measure of the amount that the light is obscured by dust. In our calculations of the dust temperatures (see Appendix I), the results were most consistent when we assumed an constant extinction coefficient (τ) at a wavelength of 2.2 microns. This implies a constant amount of dust in the foreground obscuring the light. Comparing the 3 GHz flux with the flux at H gave us

corrections for the dust emission in the determination of the dust temperatures. This produced extinction factors as high as 5 for some points and led to nonphysical values of temperature. With an extinction constant of 0.6, however, a sensible dust temperature map was produced with problems at only two positions, both of which are associated with very dense clouds seen on the H plates. These can be expected to be difficult to accurately model.

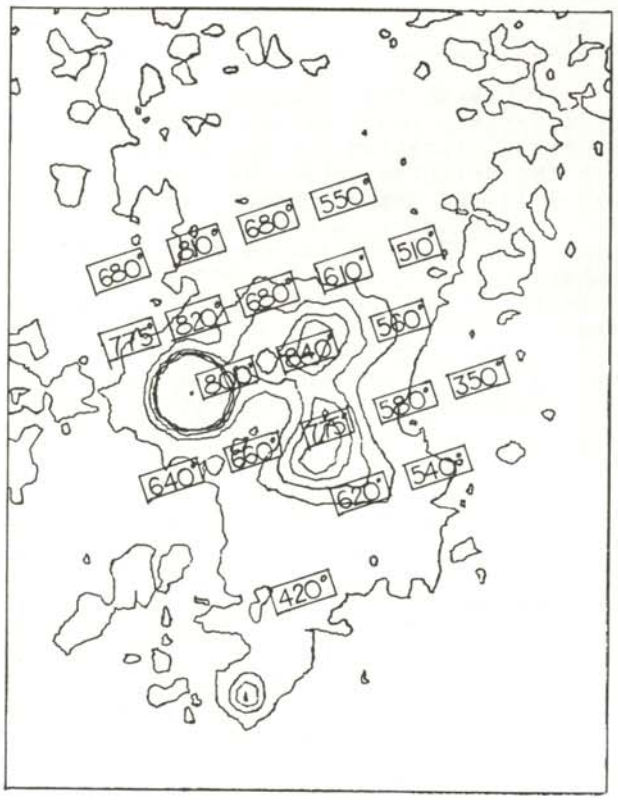

Figure 3
Color temperature map of the dust in the hourglass region of M8

Our results are also interesting in that they indicate an elevated dust temperature in both lobes of the hourglass. However, the accuracy of the method does not allow us to state more than that the hourglass appears hotter than the surrounding points. The theoretical calculation (Appendix II) indicates that all the observed points are at a significantly higher temperature than would be expected from heating only by Her 36, or Her 36 and Cor 12403. Our 2.2 micron temperatures are consistent with those found by Thronson et.al. (8) of 45 degrees K at 88 microns, and by Woolf et.al. (9) of 200 degrees K at a wavelength of 10 microns at a distance of .03 parsecs from Her 36.

This is a strong indication that there exists one or more additional heat sorces in the area, possibly protostars hidden by the hydrogen emission. The ionization of the hydrogen undoubtedly is due to Her 36, since it is the only close source with enough energy. Foreground dust probably is the explanation of the odd visual shape and location of the hourglass. Could the hourglass itself be a site of early stellar evolution? Smith and Weedman (10) calculated the upper limit of the age of the lobes from the expansion rates. The results of 3300 years for the northern lobe and 4800 years for the southern lobe certainly are within the range we are considering.

Our study of M8 has been extensive, but not complete. Further study with observations of the intensities of the spectral lines Hα , Hβ , Bα , and Bβ at points in and around the hourglass would allow the calculation of much more accurate dust temperatures. This, coupled with observations to the west of Her 36, would provide the data necessary for a more definitive model of the region.

APPENDIX I

Determination of flux from voltage output of the scanning photometer.

$$F_{source} = \frac{F_{std} \times V_s / V_{std} \times Scale_s / Scale_{std}}{\Delta magnitude}$$

Standard used: SJ 9540

Wavelength:	2.2μ(K)	3.5μ(L)
Voltage (at 1.9 air mass)	41385	10809
Magnitude	7.62	7.63

For 0 magnitude: $F_L = 0.73 \times 10^{-14} W/cm^2\mu m$

$F_K = 4.07 \times 10^{-14} W/cm^2\mu m$

Yielding a $\Delta mag = 1116.86$

So:

$F_{L,std} = 6.5 \times 10^{-18} W/cm^2\mu m$

$F_{K,std} = 3.6 \times 10^{-17} W/cm^2\mu m$

and

$$F_{L,source} = 1.21 \times 10^{-22} V_s \quad (10mv)$$

$$F_{K,source} = 1.76 \times 10^{-22} V_s \quad (10mv)$$

$$F_{K,source} = 0.86 \times 10^{-22} V_s \quad (5mv)$$

The total flux from the source is

$$F_{source} = F_{dust} + F_{gas}$$

with $F_{source} = F^{obs}_{\lambda}\, e^{\tau}_{\lambda}$, $F_{gas} = F^{ff}_{\lambda}$

so the correction for dust becomes

$$F_{\lambda,dust} = F^{obs}_{\lambda}\, e^{\tau}_{\lambda} - F^{ff}_{\lambda}$$

We know $F^{obs}_{\nu} = \alpha\, S_{\nu}\, e^{\tau IR}$

where $S_{\nu} = F_{\gamma}/(1.1 \times 10^{12}\ W/cm^2)$

and $F^{ff}_{L} = \beta_L S_V = F^{obs}_{IR}(\beta_L/\alpha)e^{\tau IR}$

$$F^{ff}_{L} = \beta_L\, S_V = F^{obs}_{IR}(\beta_L/\alpha)e^{\tau IR}$$

*Pt.	Voltage	Scale	Flux x 10^{-19} W/cm² (λ = 3.5 μ)	Voltage	Scale	Flux x 10^{-19} W/cm² (λ = 2.2 μ)
1	7036	10mv	8.54	2829	10mv	4.98
2	20440	"	24.70	10203	"	18.00
3	3339	"	4.04	1682	"	2.96
4	7227	"	8.74	4949	"	8.72
5	13814	"	16.70	9180	"	16.20
6	17914	"	21.70	10725	"	18.90
7	6793	"	8.22	3700	"	6.52
8	1753	"	2.12	1061	"	1.87
9	2070	"	2.50	1578	"	2.78
10	3775	"	4.57	2483	"	4.37
11	12041	"	14.60	5999	"	10.60
12	11511	"	13.90	8890	"	15.70
13	6494	"	7.85	6100	"	10.70
14	3519	"	4.26	2166	"	3.81
15	2498	"	3.02	1739	"	3.06
16	10526	"	12.70	3840	"	6.76
17	12193	"	14.60	3080	"	5.42
18	8991	"	10.90	2621	"	4.62
19	4571	"	5.53	1979	"	3.49
20	3676	"	4.45	914	"	1.61
21	5445	"	6.58	771	5mv	0.68
22	6258	"	7.57	1411	"	1.24

Table 1
Intensity data on the hourglass portion of M8 taken by J. Pipher on 29 July 1980. The locations are shown on Fig. 4

letting $\gamma_K = \tau_K/\tau_{IR}$ and $\gamma_L = \tau_L/\tau_{IR}$

We can write the dust corrections as

$$F^{corr}_{K,dust} = F^{obs}_{K}\,(e^{\tau IR})^{\gamma K} - F^{obs}_{IR}(\beta_K/\alpha)e^{\tau IR}$$

and a corresponding correction for the L wavelength

At a position on the plate (13) we have a spectrum. Using the observed flux for the different wavelengths yields a gas flux

$$F^{ff}_{K} = 2.97\, F_{\gamma}$$

$$F^{ff}_{L} = 1.01\, F_{\gamma}$$

and hence find the dust correction to be

$$F^{corr}_{K,dust} = F^{obs}_{K}(e^{\tau IR})^{\gamma K} - \frac{F^{obs}_{IR} e^{\tau IR}}{F(13)_{IR}\, e(13)_{IR}}\, 2.97 F_{\gamma}\, e^{\tau(13)K}$$

and a corresponding relationship for the L wavelength.

with a wavelength difference of .028 micron we get an $F_{\gamma} = 2.26 \times 10^{-19}\ W/cm^2$

Now to find τ, we use the reddening correction determined for Hβ by Peimbert and Costero (11) in their work on chemical abundances in the HII regions. For the hourglass region

$$F^{obs}_{H\beta} = F^{pred}_{H\beta} \times 10^{-C_{H\beta}} \text{ giving } C_{H\beta} = 0.52$$

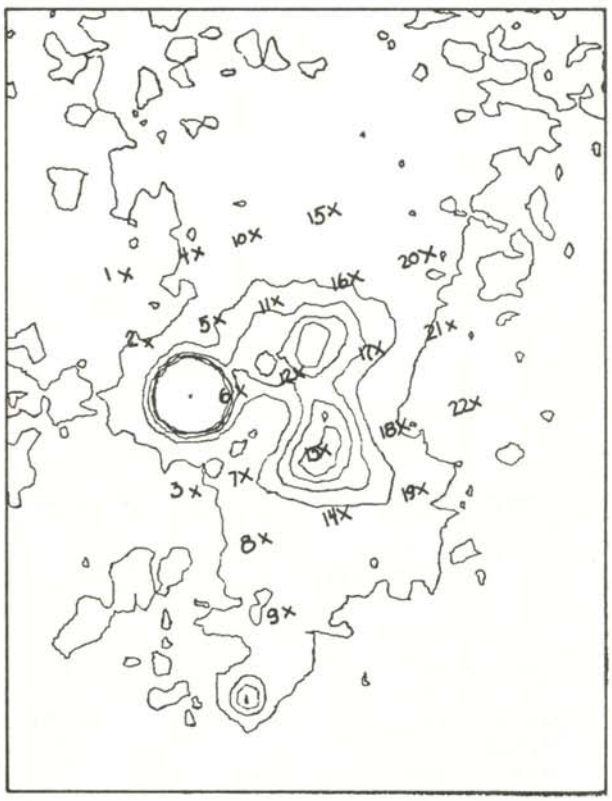

Figure 4
Locations of intensity data points listed in Table 1

so $A_{H\beta} = C_{H\beta} \times - 2.5 = -1.3$

Since $10^{-(A_\lambda/2.2)} = e^{-\tau_\lambda}$

$\tau_\lambda = A_\lambda (\ln 10/2.5) = 0.92\ A_\lambda$

Using $A_V = 3.05\ E_{H\beta - V}$ (11)

$A_{H\beta} - A_{IR} = 0.66 = 1.3 - A_{IR}$

$A_{IR} = 0.64$

yields $\tau_{IR} = 0.6$, or $e^{\tau IR} = 1.82$

The ratio FK/ FL was then entered on the graph in Fig 5 and the corresponding temperature read off. The temperature was

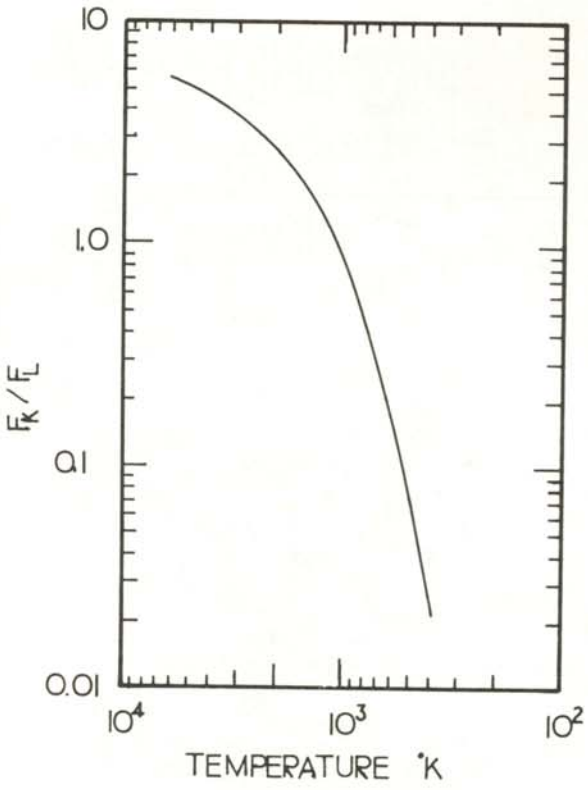

Figure 5
The ratio of Flux at a wavelength of 2.2 microns to the Flux at a wavelength of 3.5 microns vs. the Temperature of the dust. These are the results of the calculations in Appendix I.

multiplied by 2.2/3.5, the ratio of the wavelengths, to give the true black-body temperature, corrected for the separation of the points on the curve.

The error in the dust temperature was found to be $\pm$ 125K

APPENDIX II

Calculation of dust temperature in a HII region (12)

Energy balance gives

$$4\pi\int_0^\infty J_\nu(r) \langle Q_{abs}\pi a^2\rangle\, d\nu = \int_0^\infty 4\pi B_\nu(T_\alpha) \langle Q\pi a^2\rangle d\nu$$

Where J_ν is the mean intensity and $B_\nu(T_\alpha)$ the Planck function.

The mean intensity is made up of several pieces:
1) direct starlight
2) Lyman alpha photons
3) other diffuse radiation, which we will ignore.

From direct starlight

$4\pi J_\nu = \pi\ F_\nu(R)\ R^2/r^2$ where F is the radiative flux

For Lyman alpha photons the emission coefficient is:

$$j_{L\alpha} = N_e\ N_p\ (\alpha_\beta - \alpha_{2s}^{eff})h\nu_{L\alpha}$$

If we assume that all Lyman photons are absorbed by the dust in the nebula, then

$$4\pi\int j_{L\alpha} d\nu = 4\pi\int N_d Q_{L\alpha}\pi a^2 J_{L\alpha} d\nu$$

or in an "on the spot" approximation:

$$J_{L\alpha} = j_{L\alpha} / (N_d Q_{L\alpha}\pi a^2)$$

$$= N_d\ N_e(\alpha_\beta - \alpha_{2s}^{eff})h\nu_{L\alpha}/(N_d Q_{L\alpha}\pi a^2)$$

So the energy balance equation becomes

$$\pi R^2/r^2 \int F_\nu(R)\langle Q_{abs}\pi a^2\rangle d\nu + \frac{N_e N_p(\alpha_\beta - \alpha_{2s}^{eff})h\nu_{L\alpha}}{N_d}$$

Assuming for
ultraviolet $Q_{abs} = Q_{uv}(\nu/\nu_{uv})^\alpha$

infrared $Q_\nu = Q_{IR}(\nu/\nu_{IR})^\beta$

and

$$F_\nu \sim B_\nu$$

and recalling that the integral

$$\int_0^\infty \frac{x^{\alpha+3}\,dx}{e^x - 1} = \Gamma(4+\alpha)\ \zeta(4+\alpha)$$

$$= (3+\alpha)!\ \zeta(4+\alpha)$$

where the Riemann function has values

$$\zeta(4) = 1.082$$
$$\zeta(5) = 1.037$$
$$\zeta(6) = 1.017$$

we get

$$\frac{4\pi R^2}{4\pi r^2}\frac{2\pi h}{c^2}(kT/h)^{4+\alpha}(3+\alpha)!\,\zeta(4+\alpha)Q_{uv}\nu_{uv}^{-\alpha}$$

$$+N_eN_p(\alpha_\beta - \alpha_{2s}^{eff})h\nu_{L\alpha}/(N_d\pi a^2)$$

$$= 4\pi\ 2h/c^2(kT_d/h\nu_{IR})^{4+\beta}\quad \zeta(4+\beta)Q_{IR}\nu_{IR}^4(3+\beta)!$$

Note that

$$L_* = 4\pi R_*^2\ T_*^4 = 4\pi R_*^2\ 2\ h/c^2(r/h)\ 3!\zeta(4)T_*^4$$

$$\tau_{uv} = (N_d\pi a^2)(Q_{uv}r_{HII})$$

$$H_L = 4/3\pi r_s^3\alpha_\beta\ N_eN_p$$

$$(r_{HII}/r_s)^3 = e(-0.82\bar{\tau}_{uv})$$

yields $r_{HII} = (3N_L/4\pi N_eN_p\alpha_\beta)^{1/3}\ e(-0.27\bar{\tau}_{uv})$

setting $r' = r/r_{HII}$ we get

$$\left(\frac{Q_{uv}L_*}{4\pi r'^2}\right)\left(\frac{kT_K}{h\nu_{uv}}\right)\left(\frac{(3+\alpha)!\,\zeta(4+\alpha)}{6\ \zeta(4)}\right)\left(\frac{4\pi N_eN_p\alpha_\beta}{3N_L}\right)^{2/3}e(.54\bar{\tau})$$

$$+\frac{Q_{uv}N_eN_p}{\bar{\tau}_{uv}}\left(\frac{3N_L}{4\pi N_eN_p\alpha_\beta}\right)^{1/3}(\alpha_\beta - \alpha_{2s}^{ef})h\nu_{L\alpha}e(-.27\bar{\tau})$$

$$= 4\pi 2h/c^2(kT_d/h\nu_{IR})^{4+\beta}\ (3+\beta)!\,\zeta(4+\beta)Q_{IR}\nu_{IR}^4$$

This expression is then solved to find the dust temperature

$$T_d = \frac{hc}{k\lambda_{IR}}\left[\frac{Q_{uv}}{Q_{IR}}\left(\frac{\lambda_{IR}^4}{c^2 4\pi h(3+\beta)!\,\zeta(4+\beta)}\right)\left(\frac{L_*}{4\pi r^2}\right)e(r'\bar{\tau}_{uv})\frac{r_{HII}N_eN_p(\alpha_\beta - \alpha_{2s}^{eff})h\nu_{L\alpha}}{\bar{\tau}_{uv}}\right]^{1/(4+\beta)}$$

where the factor for the attenuation of the stellar flux has been added.

Putting in values for the constants in the equation for the temperature of the dust

$\lambda_{IR} = 2.2\mu m$ $\quad N_e = N_p = 6000/cm^3$

$\lambda_{uv} = 1215 \times 10^{-8}$ cm

$\alpha_\beta = 3.57 \times 10^{-13} cm^3/s$ $\quad \alpha_{2s}^{eff} = 1.1 \times 10^{-13} cm^3/s$

$L_* = 6.78 \times 10^{38}$ ergs/s for a Type 07 star such as Her 36

$N_L = 7.24 \times 10^{48}$ photons/s

$\beta = 1$ for silicates

r_{HII} approximated by the Stromgren radius:

$r_{HII} = (3N_L/(4\pi N_eN_p\alpha_\beta))^{1/3}\ \exp(-0.27\tau_{uv})$

$= 0.2 \exp(-0.27\tau_{uv})$ parsecs

yields:

$$T_d = 6540\left[3.25 \times 10^{-11}(5.67/r^2 + 450r_{HII}/\tau_{uv})\right]^{\frac{1}{5}}$$

Distance from Her 36	Temperature
parsec	K
3.2×10^{-9}	1.83×10^5
3.2×10^{-8}	7.12×10^4
3.2×10^{-5}	4.62×10^3
3.2×10^{-2}	2.93×10^2
1.6×10^{-2}	1.65×10^2
3.2×10^{-1}	1.44×10^2

Table 2
Results of distance-temperature calculations in Appendix II. Notice that at the center of the northern lobe of the M8 hourglass (.016 parsecs from Her 36), the calculated temperature is only 165 K compared to the measured value of 840 K.

Assuming that the hourglass has properties similiar to the Orion nebula, we use values

$\tau_{uv} = 0.64$ $r_{HII} = 0.15$ parsec

giving a final formula for the dust temperature:

$$T_d = 52 \left[5.67 / r^2(psc) + 105 \right]^{.2}$$

Results of the calculations are listed in Table II.

ACKNOWLEDGEMENTS

We would like to thank Dr. S. Sharpless and Dr. J Pipher for their insight and guidance during our work this year. We also recognize T. Herter and M. LaCasse with gratitude for their time and effort in assisting us with the mathematical details and in working with the computer.

REFERENCES

(1) Pipher, J., private communication.

(2) Dyck, H. M., Astronomical Journal, 82, 129 (1977); Turner, B. E., Balick, B., Cudaback, D. D., Heiles, C., and Boyle, R.J., Astrophysical Journal, 194, 279 (1975); Wink, J. E., and Altenhoff, J., Astronomy and Astrophysics, 38, 109 (1975); Zeilik, M., Astrophysical Journal, 84, 341 (1979).

(3) Thackeray, A. D., M.N.R.A.S, 110, 350 (1950).

(4) Sharpless, S., private communication.

(5) Pottasch, S. R., Vistas in Astronomy, 6, 149 (1965).

(6) Foukal, P. V., Astrophysics and Space Science, 5, 469 (1969).

(7) Elliot, K. H., and Meaburn, F., M.N.R.A.S., 172, 427 (1977).

(8) Thronson, H. A., Lowenstein, R. F., and Stokes, G. M., Astrophysical Journal, 84, 1328 (1979).

(9) Woolf, N. J., Stein, W. A., Gillet, F. C., Merrill, K. M., Becklin, E. E., Neugebauer, G., and Pepin, T. J., Astrophysical Journal, 179, 1111 (1973).

(10) Smith, M. G., and Weedman, D. W., Astrophysical Journal, 160, 65 (1970).

(11) O'Dell, C. R., Hubbard, W. B., and Peimbert, M., Astrophysical Journal, 143, 743 (1965).

(12) Herter, T., private communication.

(13) Kitt Peak National Observatory is operated by the Association of Universities for Research in Astronomy, Inc., under contract with the National Science Foundation.

SPONSOR OF THIS PAPER

Dr. S. Sharpless and Dr. J. Pipher
University of Rochester,
Rochester, NY 14627

ELECTRICAL CONDUCTIVITY IN DOPED GERMANIUM

Steven Baier
Luther College, Decorah , Iowa 52101

ABSTRACT

Measurements of conductivity as a function of temperature have been made in P-type and N-type germanium samples in the range 77 K - 375 K. The results reported here are in good agreement with theory and with work done by others. (1) A general discussion of semiconductor conduction theory is given. The parameters computed from the data are: a) the mobility in the extrinsic region; b) the germanium energy gap; c) sample acceptor/donor concentration. All values like within 2% of the accepted theoretical predictions through the temperature range 77 K - 375 K.

INTRODUCTION

Theoretically, only two factors control semiconductor conductivity: a) carrier concentration - the number of charge carriers available to transport charge in the crystal- and b) carrier mobility - the ease with which these carriers move through the crystal. This experiment demonstrates how factors influencing carrier concentration and mobility may be isolated and their effects measured.

The relationship of conductivity to charge carrier concentration and mobility is expressed as

$$\sigma = q_+ p \mu_p + q_- n \mu_n \quad \text{Equation 1}$$

where σ is the conductivity, q is the carrier charge, p and n the hole and electron populations, and μ_P and μ_N are the hole and electron mobilities. To get an experimental measurement of conductivity we use the related expression for conductivity

$$\sigma = 1/\rho = 1/(RA/L) = (L/A)(1/R)$$

Where R is the sample resistance, L is the sample length, and A is its cross-sectional area. Knowing the sample's dimensions, we can measure its resistance as a function of temperature and easily compute the conductivity.

SAMPLE PREPARATION

The samples used in this experiment were small P-type and N-type bars of single-crystal germanium (2) measuring approximately 1 mm x 1 mm x 10 mm. The P-type bar was doped with indium and the N-type sample with antimony. Exact impurity concentrations were not available.

Although germanium does not react quickly in air, it is known to form both oxides and dioxides. (3) Oxides on the surface of the semiconductor offer undesirable energy possibilities for charge carriers and must be removed as much as possible. (The oxide coating also makes a good electrical connection to the crystal difficult.) To remove these surface contaminants, the samples were etched for approximately 10 minutes in "CP4 etch" (4) and rinsed in methanol. Connections were made to each end of the samples using #28 copper wire and 50-50 solder. No rectifying behaviour was noticed in the contacts.

The P-type sample had a room temperature resistance of 496.7 ohms and a resistivity of 6.43 ohm-cm. The N-type sample had a resistance of 1010 ohms and resistivity of 7.92 ohm-cm. (Pure germanium has a resistivity of 43 ohm-cm.) (5)

APPARATUS

The apparatus used in this experiment was designed to create the necessary temperature environment for the samples (70 - 375 K) with readily available equipment. The germanium sample and thermocouple were mounted on the bottom of a small aluminum chamber in thermal compound to maintain them at approximately the same temperature. The chamber was placed inside a well-insulated calorimeter so that the liquid nitrogen coolant added inside would boil off and let the chamber warm up naturally. The chamber reached -195 C in about 90 seconds and warmed to to 0 C in 30 minutes.

To explore conductivity in the temperature range 0 - 100 C, a power

resistor was placed in contact with the bottom of the calorimeter, alongside the sample chamber. The resistor was supplied by a Variac. It was found that 15 watts raised the sample temperature from 0 C to 110 C in 25 minutes.

The basic experimental method was to measure simultaneously the resistance of the sample and its temperature as the sample chamber warmed up. Sample resistance was measured with a digital ohmeter. A calibrated iron-constantan thermocouple and a digital voltmeter were used to measure the chamber temperature. The measurements were made every 60 sec. The data were entered into a computer program which generated sample conductivity and absolute reciprocal temperature for each measurement. These data were then plotted directly.

EXPERIMENTAL RESULTS

A doped semiconductor is unique in that it has two possible sources of charge carriers. First there are the carriers purposely added to the crystal by doping. (Dopant atoms called "acceptors" add positive holes to the carrier population and make the material P-type, while "donor" atoms add negative electrons and make the material N-type.) These "extra" carriers are weakly bound to their dopant atoms and may be freed easily (with energy on the order of .01 eV). This is called extrinsic conduction. Secondly, there are electron-hole pairs created by exciting the electrons of the germanium atoms themselves to higher energy states. (This is basically the mechanism which provides conductivity in other non-metallic substances.) These electrons (and holes) are bound more tightly to their atoms and will only be released by considerably more energy than needed for doped carriers (on the order of 1 eV). This is called intrinsic conduction.

Most of the energy which releases charge carriers and provides conduction comes from thermal energy, of which the temperature of the sample is a good measure. To be sure, a very high electric field or intense light on the sample will affect conductivity by liberating some carriers, but precautions were taken to prevent these conditions in the experiment. The major factor controlling carrier population, then, is temperature.

On the basis of carrier population alone, we expect the conductivity of our sample to vary as follows. At 0 K, the conductivity should be zero since no energy is available to release any charge carriers. As the sample temperature rises, the extrinsic carriers should be released, so we expect the conductivity also to rise and eventually to level off when the extrinsic carriers have all been released (about 80 K). The conductivity should then remain constant until the intrinsic carriers begin to be released (about 300 K). From 300 K up, the conductivity should rise rapidly as the germanium atoms begin to give up their electrons.

But in the introduction, we said that TWO factors control conductivity - carrier population AND mobility. We must then consider carrier mobility as well (or its inverse - carrier scattering) to obtain a reasonable qualitative picture. In the low temperature range (0 - 80 K), we find very little lattice motion and hence very little carrier scattering from collisions with out-of-place germanium atoms. However, the thermal velocities of these carriers are quite small and any impurity or fault in the crystal will deflect them significantly. This is roughly analagous to rolling a marble over a very uneven surface. Roll it slowly, and the marble will change direction many times. Roll it faster, and the marble follows a much straighter path. Unfortunately, this interesting temperataure region is quite out of the reach of our simple apparatus and no data could be gathered for it.

80 - 300 K Region

At the lowest temperature we can reach (80 K), the thermal velocities of the carriers have increased to the point that impurity scattering is no longer important and lattice or "phonon" scattering dominates. The carrier population is constant now since all extrinsic carriers have been released and sufficient thermal energy is not yet available to begin exciting the important number of intrinsic carriers. If the carrier population is constant, the observable conductivity really depends only on carrier mobility. By observing conductivity in this range, we can directly measure the influence of temperature on carrier mobility.

As an example, take N-type germanium in the temperature range 80 K - 300 K. Here the only carriers are extrinsic electrons. Thus $p = 0$ and n is constant once all donor electrons have been released. Crudely speaking, we might

expect

$$\sigma \propto \mu_n \propto 1/(\text{collision frequency})$$

$$\propto 1/(\text{thermal velocity} \times \text{phonon density})$$

$$\propto 1/((3kT/m)^{.5}\, T)$$

In other words, we might expect the mobility (i.e. the conductivity) in this region to vary as $T^{-1.5}$. A more rigorous derivation by Bardeen and Shockley (6) gives the lattice mobility as

$$\mu_L = \frac{(8\pi)^{.5} h^4 c_{11}}{3 E_{1n}^2 m_n (kT)^{3/2}} \propto T^{-1.5}$$

Where the terms c_{11}, E_{1n}, m_n are certain constants that depend slightly on temperature. The accepted experimental values of mobility temperature dependence (7) for germanium is $T^{-1.66}$ in N-type material and $T^{-2.33}$ in P-type material. We measured values of the temperature exponent of -1.68+/-.02 for N-type and -2.080+/-.006 for the P-type. These values were determined by finding the slope of the log-log plot of conductivity vs 1/T in this temperature range. Other sources (8) give P-type temperature dependences of -2.00 and -2.08, much closer to our value.

300-375 K Region

At room temperature and above, lattice scattering continues as before, but now enough energy is becoming available to excite a significant number of valence electrons (intrinsic carriers) into higher energy states, so the carrier population grows rapidly. In fact, the intrinsic population, Ni, is known to depend exponentially on temperature and has the form (9)

$$N_i = 2(2\pi kT/h^2)^{3/2} (m_p m_n)^{3/4} \exp(-E_g/2kT)$$

Where Eg is the size of the energy gap. This expression is essentially the effective density of available energy states multiplied by the Fermi probability of occupancy. Because of the sharp temperature dependence, the number of intrinsic carriers grows very quickly once sufficient thermal energy is available. Since there are so many more intrinsic than doped carriers (often a million tc one or more), the extrinsic population becomes negligible. In fact, the growth of Ni is so rapid that it overwhelms the scatting mechanisms as well and we see a purely exponential rise in conduction on the Graphs 1a and 1b. The temperature at which conductivity begins to rise sharply due to the intrinsic carrier boom was 45 C in the P-type and 33 C in the N-type samples.

The complete picture of conductivity as a function of temperature is shown in Graph 1. All data for each type of sample was compiled and plotted together here. The error bars represent scatter among the data of different runs and the empty circles indicate data points found in one run only, that is, data not confirmed by subsequent runs.

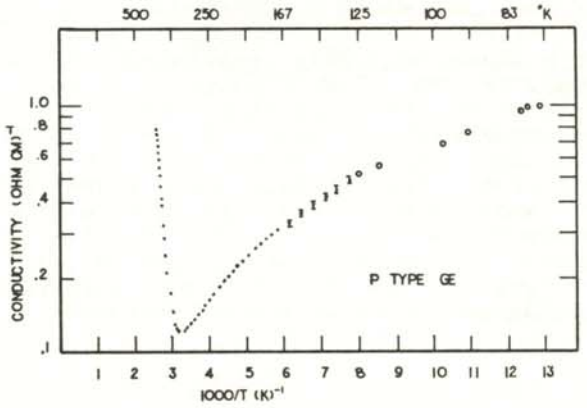

Figure 1a
Conductivity in P-type germanium. Complilation of all data. Error bars indicate scatter, empty circles denote data gathered by only one run.

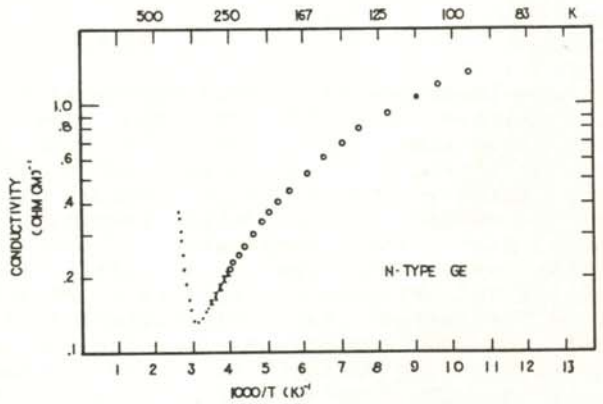

Figure 1b
Conductivity in N-type germanium. Compilation of all data. Error bars indicate scatter, empty circles denote data gathered by only one run.

There is still some information to be gathered from this data. In the intrinsic region (300-400 K), p=n=Ni (see eqtn 1) since the carriers were created in pairs. and are essentially constant in the range since scattering is made negligible by the rapid increase in Ni. Then

$$\sigma \propto N_i \propto \exp(-E_g/2kT)$$

where Eg is the energy gap. By plotting $\ln(\sigma)$ vs 1/T, we should get a slope equal to -Eg/(2k) and then can find a value for the energy gap. The accepted value for Eg for germanium is 0.67 eV, for the axis along which our measurement was made. (10) We found a value for the energy gap of 0.684+/-.009 eV.

Since no doping concentrations were available for the crystals, it would be interesting to calculate the value from our experimental data and see if it falls in the usual range of 10^{13} to 10^{16} atoms/cm^3. The obvious temperature range for this computation is the extrinsic region (80 - 300 K), since essentially no intrinsic carriers would yet exist and conductivity is totally due to extrinsic conduction. Here equation 1 becomes

$$\sigma = q\_n\mu_n$$

for an N-type material. Since the expression for mobility given by Bardeen and Shockley is rather complicated, we will make use of a simpler approximation developed by Conwell (11)

$$\mu \approx 1.05 \times 10^9 \, T^{-2.33} \quad (125 - 300K)$$

$$\mu \approx 4.9 \times 10^7 \, T^{-1.66} \quad (100 - 300K)$$

At room temperatures, these approximations give values only 5% off the accepted mobilities quoted in (11). To use the approximations in our case, we chose a temperature in the intrinsic region, found the conductivity at that temperature, substituted the temperature into the approximation to get a mobility. We arrived at impurity concentrations of 4.66×10^{14} holes/cm^3 for P-type material and 2.06×10^{14} electrons/cm^3 for N-type material. The mobility approximation made these calculations meaningful only to the order of magnitude.

ACCURACY OF MEASUREMENTS

There are several important sources of possible error in this experiment. One is in measuring the sample temperature. Since this is a key variable in the analysis, the temperature of the sample must be measured very accurately. This was considered in the design of the apparatus by mounting both sample and thermocouple on a relatively large metal surface to assure good temperature stability. We do, however, assume that the sample and the thermocouple cool and warm at the same rate. Several factors make this assumption questionable. The masses and specific heats of the two are dissimilar, and perhaps more importantly, the germanium bar has more surface are in direct contact with the metal surface than the thermocouple because of its shape. A temperature differetial was actually observed while taking the data: the room temperature resistance of the sample was always taken before the sample was placed in the apparatus, and this value compared with the value read as the sample chamber passed room temperature on its way to 100 C. The resistance during the test was high by 1.5%. That is, the sample temperature appeared to be 1.5 C higher than the thermocouple. This difference is, however, much too small to affect the computations.

A second possible source of error is in the contacts made to the germanium crystal. Since the digital ohmeter that measured the sample's resistance uses Ohm's law, it is essential that the sample's contacts are completely ohmic over all temperataure ranges and do not rectify as the usual MOS junctions do. To test this, one run was made in which the sample's resistance was measured by applying a known voltage across the sample and measuring the current passing through. The current was limited to give a maximum of 1 mw heating to the germanium crystal. Data were taken in the temperature range 0 C - 101 C, the most critical range for soldered contacts.

ACKNOWLEDGEMENTS

Thanks go to Mr. Thomas Carroll of Crystal Tech Associates for his kindness in providing the germanium crystals. Special thanks to Miss Tamela Uphoff for her invaluable assistance in preparing the samples.

REFERENCES

(1) Debye and Conwell, Phys. Rev. 93, 693 (1954); Conwell, Proc. IRE, 46 (June 1958), p. 1281-1300.

(2) Obtained from Crystal Tech Associates, 210 Redman Ave., Haddonfield, NJ 08033.

(3) Handbook of Chemistry and Physics, 56th edition, 1975, CRC Press, p. B-17

(4) Melissinos, Experiments in Modern Physics, 1966, p.90; Haynes and Shockley, Phys. Rev. 81, 838 (1951).

(5) Handbook of Chemistry and Physics, 56th edition, 1975, CRC Press, p. B-17

(6) Debye and Conwell, Phys. Rev. 93, 696 (1954).

(7) Debye and Conwell, Phys. Rev. 93, 693 (1954); Adler, Smith, and Longini, Introduction to Semiconductor Physics, 1964, p. 35.

(8) Adeler, Smith, and Longini, Introduction to Semiconductor Physics, 1964, p.34; Melissinos, Experiments in Modern Physics, 1966 p.94.

(9) Streetman, Solid State Electronic Devices, 1980, p.77.

(10) Streetmen, Solid State Electronic Devices, 1980, p. 443.

(11) Conwell, Proc. IRE, 46, (June 1958), p. 1281- 1300.

SPONSOR FOR THIS PAPER
Dr. Dennis Barnaal
Luther College, Decorah, Iowa, 521001